

RAPID COAGULATION OF POROUS DUST AGGREGATES OUTSIDE THE SNOW LINE: A PATHWAY TO SUCCESSFUL ICY PLANETESIMAL FORMATION

SATOSHI OKUZUMI¹, HIDEKAZU TANAKA², HIROSHI KOBAYASHI¹, AND KOJI WADA³

ApJ, in press

ABSTRACT

Rapid orbital drift of macroscopic dust particles is one of the major obstacles against planetesimal formation in protoplanetary disks. We reexamine this problem by considering porosity evolution of dust aggregates. We apply a porosity model based on recent N -body simulations of aggregate collisions, which allows us to study the porosity change upon collision for a wide range of impact energies. As a first step, we neglect collisional fragmentation and instead focus on dust evolution outside the snow line, where the fragmentation has been suggested to be less significant than inside the snow line because of a high sticking efficiency of icy particles. We show that dust particles can evolve into highly porous aggregates (with internal densities of much less than 0.1 g cm^{-3}) even if collisional compression is taken into account. We also show that the high porosity triggers significant acceleration in collisional growth. This acceleration is a natural consequence of particles' aerodynamical property at low Knudsen numbers, i.e., at particle radii larger than the mean free path of the gas molecules. Thanks to this rapid growth, the highly porous aggregates are found to overcome the radial drift barrier at orbital radii less than 10 AU (assuming the minimum-mass solar nebula model). This suggests that, if collisional fragmentation is truly insignificant, formation of icy planetesimals is possible via direct collisional growth of submicron-sized icy particles.

Subject headings: dust, extinction — planets and satellites: formation — protoplanetary disks

1. INTRODUCTION

Growth of dust particles is a key process in protoplanetary disks. Current theories of planet formation assume kilometer-sized solid bodies called “planetesimals” to form from dust contained in protoplanetary disks. Being the dominant component of disk opacity, dust also affects the temperature and observational appearance of the disks. Furthermore, dust particles are known to efficiently capture ionized gas particles in the gas disk, thereby controlling magnetohydrodynamical behaviors of it (Sano et al. 2000).

Theoretically, however, it is poorly understood how the dust particles evolve into planetesimals. One of the most serious obstacles is the radial inward drift of macroscopic aggregates due to the gas drag (Whipple 1972; Adachi et al. 1976; Weidenschilling 1977). Because of the gas pressure support in addition to the centrifugal force, protoplanetary disks tend to rotate at sub-Keplerian velocities. By contrast, dust particles are free from the pressure support, and hence they tend to rotate faster than the gas disk. The resulting head wind acting on the dust particles extracts their angular momentum and thus causes their drift motion toward the central star. In order to go beyond this “radial drift barrier,” dust particles must decouple from the gas drag (i.e., grow large) faster than they drift inward. However, previous work by Brauer et al. (2008a) showed that dust particles finally fall onto the central star unless the initial dust-to-gas mass ratio is considerably higher than the canonical interstellar value.

Several mechanisms have been raised so far regarding how dust particles overcome the radial drift barrier. A classical idea is that dust particles “jump” across the barrier

by forming a gravitationally unstable thin dust layer at the midplane and directly collapsing into planetesimal-size objects (Safronov 1969; Goldreich & Ward 1973; Hayashi et al. 1985). However, this classical scenario has been challenged by the fact that the dust layers are easily stirred up by disk turbulence (Weidenschilling & Cuzzi 1993; Turner et al. 2010). Moreover, the dust sublayer is known to induce the Kelvin-Helmholtz instability, which prevents further sedimentation of dust even without disk turbulence unless the dust-to-gas surface density ratio is considerably high (Sekiya 1998). Recently, a two-fluid instability of dust and gas has been discovered (Youdin & Goodman 2005), which can lead to fast formation of gravitationally bound dust clumps (e.g., Johansen & Youdin 2007; Johansen et al. 2007; Bai & Stone 2010a). However, this mechanism requires marginally decoupled dust particles, the formation of which is already questioned by the radial drift barrier itself. Other possibilities include the trapping of dust particles in vortices (e.g., Barge & Sommeria 1995; Klahr & Henning 1997) and at gas pressure maxima (e.g., Kretke & Lin 2007; Brauer et al. 2008b; Suzuki et al. 2010; Pinilla et al. 2012).

This study reexamines this problem by considering a new physical effect: porosity evolution of dust aggregates. Most previous coagulation models (e.g., Nakagawa et al. 1981; Tanaka et al. 2005; Brauer et al. 2008a; Birnstiel et al. 2010) assumed that dust particles grow with a fixed internal density. In reality, however, the internal density of aggregates does change upon collision depending on the impact energy. The evolution of porosity directly affects the growth history of the aggregates since the porosity determines the coupling of them to the gas motion. For example, Ormel et al. (2007) and Zsom et al. (2011) simulated dust growth with porosity evolution at fixed disk orbital radii and found that porous evolution delays the settling of dust onto the disk midplane. However, how the porosity evolution affects the radial drift barrier has been unaddressed so far.

¹ Department of Physics, Nagoya University, Nagoya, Aichi 464-8602, Japan; okuzumi@nagoya-u.jp

² Institute of Low Temperature Science, Hokkaido University, Sapporo 060-0819, Japan

³ Planetary Exploration Research Center, Chiba Institute of Technology, Narashino, Chiba 275-0016, Japan

It has been studied over last two decades how the internal structure changes upon collision by laboratory (e.g., Blum & Wurm 2000; Weidling et al. 2009) and numerical (e.g., Dominik & Tielens 1997; Wada et al. 2008; Suyama et al. 2008, 2012) collision experiments. One robust finding of these studies is that aggregates grow into low-density, fractal objects if the impact energy is lower than a threshold E_{roll} determined by material properties (Blum & Wurm 2000; Suyama et al. 2008; Okuzumi et al. 2009). The fractal dimension d_f of the resulting aggregates depends weakly on the size ratio between targets and projectiles, and falls below two when the target and projectile have similar sizes (Mukai et al. 1992; Okuzumi et al. 2009). The fractal dimension of two is equivalent to an internal density decreasing inversely proportional to the aggregate radius. The density decrease occurs because each merger event involves the creation of “voids” whose volume is comparable to those of the aggregates before merger (Okuzumi et al. 2009). Suyama et al. (2008) estimated the collision energy of aggregates in protoplanetary disks as a function of size, and showed that aggregates composed of $0.1\mu\text{m}$ sized particles undergo fractal growth in planet-forming regions until their size reaches centimeters. This means that the building blocks of planetesimals should have once evolved into very fluffy objects with mean internal densities many orders of magnitude lower than the solid material density.

More strikingly, recent N -body experiments suggest that the porosity of aggregates can be kept considerably high even after the collision energy exceeds the threshold E_{roll} . Wada et al. (2008) numerically simulated head-on collisions between equal-sized fractal aggregates of $d_f \approx 2$ and found that the fractal dimension after the collision does not exceed 2.5 even at high collision energies. Suyama et al. (2008) confirmed this by repeating head-on collisions of the resulting aggregates at fixed collision velocities. Furthermore, compaction is even less efficient in offset collisions, where the collision energy is spent for stretching rather than compaction of the merged aggregate (Wada et al. 2007; Paszun & Dominik 2009). These results mean that the creation of voids upon merger is nonnegligible even when the impact energy is large; in other words, the voids are only imperfectly crushed in collisional compaction. Because of technical difficulty, these theoretical predictions have not yet been well tested by laboratory nor microgravity experiments. Nevertheless, it is worth investigating how aggregates grow and drift inward if they evolve into highly porous objects.

In this study, we simulate the temporal evolution of the radial size distribution of aggregates using the advection-coagulation model developed by Brauer et al. (2008a). Unlike the previous work, we allow the porosities of aggregates to change upon collision, depending on their impact energies. To do so, we adopt the “volume-averaging method” proposed by Okuzumi et al. (2009). In this method, aggregates of equal mass are regarded as having the same volume (or equivalently, the same internal density) at each orbital distance, and the advection-coagulation equation for the averaged volume is solved simultaneously with that for the radial size distribution. To determine the porosity change upon collisional sticking, we use an analytic recipe presented by Suyama et al. (2012) that well reproduces the collision outcomes of recent N -body simulations (Wada et al. 2008; Suyama et al. 2008) as a function of the impact energy. These theoretical tools allow us to study for the first time how the porosity evolution affects the growth and radial drift of dust aggregates in protoplanetary

disks.

In order to clarify the role of porosity evolution, we ignore many other effects relevant to aggregate collision, including Coulomb interaction (Okuzumi 2009; Okuzumi et al. 2011a,b; Matthews et al. 2012), bouncing (Zsom et al. 2010, 2011; Windmark et al. 2012), and collisional fragmentation (Brauer et al. 2008a,b; Birnstiel et al. 2009, 2012). Coulomb repulsion due to negative charging can significantly slow down the initial fractal growth, but may be negligible once the collisional compaction becomes effective (Okuzumi et al. 2011b). Bouncing is often observed in laboratory experiments for relatively compact (filling factor $\gtrsim 0.1$) aggregates, but is less likely to occur when aggregates are highly porous as we consider in this study (Langkowski et al. 2008; Wada et al. 2011). Seemingly more problematic is fragmentation at high-speed collisions. This is particularly so when the aggregates are mainly composed of silicate particles, for which catastrophic disruption begins at collision speeds as low as a few m s^{-1} (Blum & Wurm 2008; Wada et al. 2009; Güttler et al. 2010). By contrast, collisional fragmentation may be less problematic for aggregates made of icy particles, for which a higher sticking threshold has been anticipated (Chokshi et al. 1993; Dominik & Tielens 1997; Gundlach et al. 2011). For instance, N -body collision experiments by Wada et al. (2009) suggest that aggregates made of $0.1\mu\text{m}$ sized icy grains do not experience catastrophic disruption at collision velocities up to $35\text{--}70\text{ m s}^{-1}$. For this reason, instead of neglecting collisional fragmentation, we focus on dust evolution *outside the snow line* in protoplanetary disks. A more comprehensive model including the above mentioned effects will be presented in future work.

We will show that dust particles evolve into highly porous aggregates even if collisional compaction is taken into account. Furthermore, we will show that the porosity evolution triggers significant acceleration in collisional growth at early stages, allowing them to grow across the radial drift barrier in inner regions of protoplanetary disks. Interestingly, this acceleration involves neither enhancement of the collision velocity nor suppression of the radial drift speed of marginally decoupled aggregates. As we will see, this acceleration is a natural consequence of particles’ aerodynamical property at low Knudsen numbers, i.e., at particle radii larger than the mean free path of the gas molecules, and the porosity evolution only allows the dust aggregates to reach that stage with small aggregate masses. Our model calculation shows that the breakthrough of the radial drift barrier can occur in “planet-forming” regions, i.e., at $< 10\text{ AU}$ from the central star. This result suggests that, if the fragmentation of icy aggregates is truly negligible, the formation of icy planetesimals is possible via direct collisional growth of dust particles even without an enhancement of the initial dust-to-gas mass ratio.

This paper is organized as follows. In Section 2, we describe the disk and collision models that we use in this study. Simulation results are presented in Section 3, which we interpret in terms of the timescales for collisional growth and radial inward drift in Section 4. The validity and limitations of our model are discussed in Section 5, and our conclusions are presented in Section 6.

2. MODEL

2.1. Disk Model

We adopt the minimum-mass solar nebula (MMSN) model of Hayashi (1981) with a solar-mass central star. The ra-

dial profiles of the gas surface density Σ_g and disk temperature T are given by $\Sigma_g = 152(r/5 \text{ AU})^{-3/2} \text{ g cm}^{-2}$ and $T = 125(r/5 \text{ AU})^{-1/2} \text{ K}$, respectively, where r is the distance from the central star. In this study, we focus on dust evolution outside the snow line, which is located at $r \approx 3 \text{ AU}$ in the adopted disk model. The vertical structure is assumed to be in hydrostatic equilibrium, and hence the vertical structure of the gas density ρ_g is given by $\rho_g = (\Sigma_g / \sqrt{2\pi} h_g) \exp(-z^2/2h_g^2)$, where $h_g = c_s/\Omega$ is the gas scale height, c_s is the isothermal sound speed, and Ω is the Kepler frequency. The isothermal sound speed is given by $c_s = \sqrt{k_B T / m_g}$, where k_B is the Boltzmann constant and m_g is the mean molecular mass. We assume the mean molecular weight of 2.34, which gives $m_g = 3.9 \times 10^{-24} \text{ g}$ and $c_s = 6.7 \times 10^4 (r/5 \text{ AU})^{-1/4} \text{ cm s}^{-1}$. The assumed stellar mass ($1 M_\odot$) leads to $\Omega = \sqrt{GM_\odot/r^3} = 1.8 \times 10^{-8} (r/5 \text{ AU})^{-3/2} \text{ rad s}^{-1}$ and $h_g/r = 0.05 (r/5 \text{ AU})^{1/4}$, where G is the gravitational constant.

In reality, protoplanetary disks can be heavier than the MMSN. The gravitational stability criterion (Toomre 1964) $\Sigma_g < \Omega c_s / \pi G \approx 5.6 \times 10^3 (r/5 \text{ AU})^{-7/4} \text{ g cm}^{-2}$ allows the surface density to be up to about 10 times higher than the MMSN value. The dependence of our result on the disk mass will be analytically discussed in Section 4.

Initial dust particles are modeled as compact spheres of equal size $a_0 = 0.1 \mu\text{m}$ and equal internal density $\rho_0 = 1.4 \text{ g cm}^{-3}$, distributed in the disk with a constant dust-to-gas surface density ratio $\Sigma_d/\Sigma_g = 0.01$. The mass of each initial particle is $m_0 = (4\pi/3)\rho_0 a_0^3 = 5.9 \times 10^{-15} \text{ g}$. In the following, we will refer to the initial dust particles as “monomers.” We define the radius of a porous aggregate as $a = [(5/6N) \sum_{i=1}^N \sum_{j=1}^N (\mathbf{x}_i - \mathbf{x}_j)^2]^{1/2}$, where N is the number of the constituent monomers and \mathbf{x}_k ($k = 1, 2, \dots, N$) is the position of the monomers (Mukai et al. 1992). This definition is in accordance with previous N -body experiments (Wada et al. 2008; Suyama et al. 2008; Okuzumi et al. 2009) which our porosity model is based on (see Section 2.3.1).

Disk turbulence affects the collision and sedimentation of dust particles. To include these effects, we consider gas turbulence in which the turnover time and mean-squared random velocity of the largest turbulent eddies are given by $t_L = \Omega^{-1}$ and $\delta v_g^2 = \alpha_D c_s^2$, respectively, where α_D is the dimensionless parameter characterizing the strength of the turbulence. The assumption for t_L is based on theoretical anticipation for turbulence in Keplerian disks (Dubrulle & Valdetaro 1992; Fromang & Papaloizou 2006; Johansen et al. 2006). The diffusion coefficient for the gas is given by $D_g = \delta v_g^2 t_L = \alpha_D c_s^2 / \Omega$. If the gas diffusion coefficient is of the same order as the turbulent viscosity, α_D is equivalent to the so-called alpha parameter of Shakura & Sunyaev (1973). However, we do not consider the viscous evolution of the gas disk for simplicity. We adopt $\alpha_D = 10^{-3}$ in our numerical simulations. A higher value of α_D would cause catastrophic collisional fragmentation of aggregates, which is not considered in this study (see Section 5.3).

2.2. Evolutionary Equations

We solve the evolution of the radial size distribution of dust aggregates using the method developed by Brauer et al. (2008a). This method assumes the balance between sedimentation and turbulent diffusion of aggregates in the vertical direction. Thus, the vertical number density distribution of

aggregates is given by a Gaussian $(N / \sqrt{2\pi} h_d) \exp(-z^2/2h_d^2)$, where $N(r, m)$ is the column number density of aggregates per unit mass and $h_d(r, m)$ is the scale height of aggregates at orbital radius r and with mass m (Dubrulle et al. 1995). This approach is valid if the coagulation timescale is longer than the settling/diffusion timescale, which is true except for very tiny particles with short collision times (Zsom et al. 2011).

The evolution of the radial size distribution $N(r, m)$ is given by the vertically integrated advection-coagulation equation, which reads (Brauer et al. 2008a)

$$\begin{aligned} \frac{\partial N(r, m)}{\partial t} = & \frac{1}{2} \int_0^m K(r, m', m - m') N(r, m') N(r, m - m') dm' \\ & - N(r, m) \int_0^\infty K(r, m, m') N(r, m') dm' \\ & - \frac{1}{r} \frac{\partial}{\partial r} [rv_r(r, m) N(r, m)], \end{aligned} \quad (1)$$

where v_r is the radial drift velocity and K is the vertically integrated collision rate coefficient given by

$$K(r, m_1, m_2) = \frac{\sigma_{\text{coll}}}{2\pi h_{d,1} h_{d,2}} \int_{-\infty}^{\infty} \Delta v \exp\left(-\frac{z^2}{2h_{d,12}^2}\right) dz. \quad (2)$$

Here, σ_{coll} is the collisional cross section, $h_{d,1}$ and $h_{d,2}$ are the scale heights of the colliding aggregates 1 and 2, Δv is the collision velocity, and $h_{d,12} = (h_{d,1}^2 + h_{d,2}^2)^{-1/2}$. As mentioned in Section 1, we neglect electrostatic and gravitational interactions between colliding aggregates and assume perfect sticking upon collision. Thus, the collisional cross section is simply given by $\sigma_{\text{coll}} = \pi(a_1 + a_2)^2$, where a_1 and a_2 are the radii of the colliding aggregates. The validity of neglecting fragmentation will be discussed in Section 5.3.

The dust scale height h_d in sedimentation-diffusion equilibrium has been analytically obtained by Youdin & Lithwick (2007). For turbulence of $t_L = \Omega^{-1}$ and $D_g = \alpha_D c_s^2 / \Omega$, it is given by

$$h_d = h_g \left(1 + \frac{\Omega t_s}{\alpha_D} \frac{1 + 2\Omega t_s}{1 + \Omega t_s}\right)^{-1/2}, \quad (3)$$

where t_s is the stopping time of the aggregates. We use this expression in this study.

For the stopping time, we use

$$t_s = \begin{cases} t_s^{(\text{Ep})} \equiv \frac{3m}{4\rho_g v_{\text{th}} A}, & a < \frac{9}{4} \lambda_{\text{mfp}}, \\ t_s^{(\text{St})} \equiv \frac{4a}{9\lambda_{\text{mfp}}} t_s^{(\text{Ep})}, & a > \frac{9}{4} \lambda_{\text{mfp}}, \end{cases} \quad (4)$$

where $v_{\text{th}} = \sqrt{8/\pi} c_s$ and λ_{mfp} are the thermal velocity and mean free path of gas particles, respectively, and A is the projected area of the aggregate. The mean free path is related to the gas density as

$$\lambda_{\text{mfp}} = \frac{m_g}{\sigma_{\text{mol}} \rho_g}, \quad (5)$$

where $\sigma_{\text{mol}} = 2 \times 10^{-15} \text{ cm}^2$ is the collisional cross section of gas molecules. Our gas disk model gives $\lambda_{\text{mfp}} = 120 (r/5 \text{ AU})^{11/4} \text{ cm}$ at the midplane. Equation (4) satisfies the requirement that the stopping time must obey Epstein's law $t_s = t_s^{(\text{Ep})}$ at $a \ll \lambda_{\text{mfp}}$ and Stokes' law $t_s = t_s^{(\text{St})}$ at $a \gg \lambda_{\text{mfp}}$, respectively. Since $t_s^{(\text{St})} \propto a t_s^{(\text{Ep})}$, an aggregate growing in the Stokes regime decouples from the gas motion more quickly

than in the Epstein regime. In reality, Stokes' law breaks down when the particle Reynolds number (the Reynolds number of flow around the particle) is much greater than unity, but we neglect this in our simulations for simplicity. We will discuss this point further in Section 5.1.

The radial drift velocity is taken as

$$v_r = -\frac{2\Omega t_s}{1 + (\Omega t_s)^2} \eta v_K, \quad (6)$$

where

$$2\eta \equiv -\left(\frac{c_s}{v_K}\right)^2 \frac{\partial \ln(\rho_g c_s^2)}{\partial \ln r} \quad (7)$$

is the ratio of the pressure gradient force to the stellar gravity in the radial direction and $v_K = r\Omega$ is the Kepler velocity (Adachi et al. 1976; Weidenschilling 1977; Nakagawa et al. 1986). The radial drift speed has a maximum ηv_K , which is realized when $\Omega t_s = 1$. In our disk model, η scales with r as $\eta = 4.0 \times 10^{-3} (r/5 \text{ AU})^{1/2}$, and the maximum inward speed $\eta v_K = 54 \text{ m s}^{-1}$ is independent of r . Since η is proportional to the gas temperature, the maximum drift speed would be somewhat lower in colder disk models (Kusaka et al. 1970; Hirose & Turner 2011). Equation (6) neglects the frictional backreaction from dust to gas assuming that the local dust-to-gas mass ratio is much lower than unity or the stopping time of aggregates dominating the dust mass is much longer than Ω^{-1} . We examine the validity of this assumption in Section 5.2.1.

In this paper, we also consider the collisional evolution of aggregate porosities. We treat the mean volume $V = (4\pi/3)a^3$ of aggregates with orbital radius r and mass m as a time-dependent quantity. The evolutionary equation for $V(r, m)$ is given by

$$\begin{aligned} \frac{\partial (VN)}{\partial t} = & \frac{1}{2} \int_0^m [V_{1+2}K](r, m', m - m') \\ & \times N(r, m') N(r, m - m') dm' \\ & - V(r, m) N(r, m) \int_0^\infty K(r, m, m') N(r, m') dm' \\ & - \frac{1}{r} \frac{\partial}{\partial r} [rv_r(r, m) V(r, m) N(r, m)], \end{aligned} \quad (8)$$

where

$$[V_{1+2}K](r, m_1, m_2) = \frac{\sigma_{\text{coll}}}{2\pi h_{d,1} h_{d,2}} \int_{-\infty}^{\infty} V_{1+2} \Delta v \exp\left(-\frac{z^2}{2h_{d,12}^2}\right) dz \quad (9)$$

with V_{1+2} being the volume of merged aggregates (described in Section 2.3.1). Equation (8) is identical to the original evolutionary equation for V derived by Okuzumi et al. (2009, their Equation (16)) except that we here take the vertical integration of the equation and take into account the radial advection of dust. In deriving Equation (8), we have assumed that the dispersion of the volume is sufficiently narrow at every r and m (see Okuzumi et al. 2009). This “volume-averaging” approximation allows to follow the porosity evolution of aggregates without solving higher-order moment equations for the volume, and hence with small computational costs. This approximation is valid unless the porosity distribution at fixed r and m is significantly broadened by, e.g., collisional fragmentation cascades (Okuzumi et al. 2009).

2.3. Dust Model

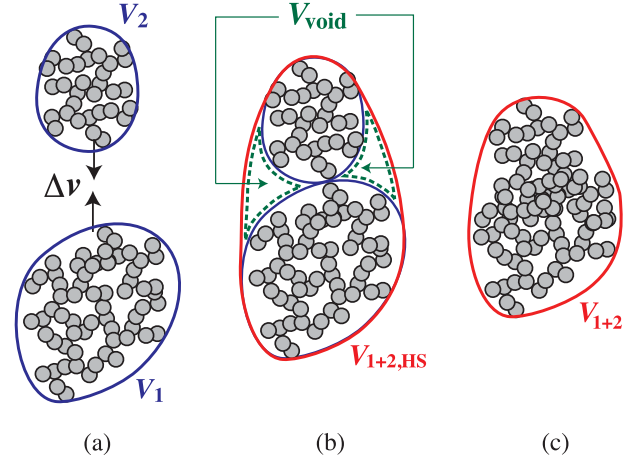


Figure 1. Schematic illustration of our porosity change model. (a) Porous aggregates with volumes V_1 and V_2 before contact. (b) Just after contact. At this moment, the volume of the new aggregate is given by $V_{1+2,HS} = V_1 + V_2 + V_{\text{void}}$, where $V_{\text{void}} = V_{\text{void}}(V_1, V_2)$ is the volume of newly formed voids (Equation (11)). If the collision energy E_{imp} is much smaller than the rolling energy E_{roll} , the final volume of the new aggregate is equal to $V_{1+2,HS}$. (c) If $E_{\text{imp}} \geq E_{\text{roll}}$, collisional compression occurs. In this case, the final volume $V_{1+2} (< V_{1+2,HS})$ depends on E_{imp} .

2.3.1. Porosity Change Recipe

The functional form of V_{1+2} determines the evolution of aggregate porosities in our simulation. In this study, we give V_{1+2} as a function of the volumes of the colliding aggregates, $V_1 = V(r, m_1)$ and $V_2 = V(r, m_2)$, and the impact energy $E_{\text{imp}} = m_1 m_2 \Delta v^2 / [2(m_1 + m_2)]$. Before introducing the final form of our porosity change recipe (Equation (15)), we briefly review recent N -body collision experiments which our recipe is based on.

Collisional compression depends on the ratio between E_{imp} and the “rolling energy” E_{roll} (Dominik & Tielens 1997; Blum & Wurm 2000; Wada et al. 2007). The rolling energy is defined as the energy needed for one monomer to roll over 90° on the surface of another monomer in contact (Dominik & Tielens 1997). When $E_{\text{imp}} \ll E_{\text{roll}}$, two aggregates stick without visible restructuring (so-called hit-and-stick collision; see Figure 1(b)). In this case, the volume of the merged aggregate is determined in a geometric manner, i.e., independently of E_{imp} . When $E_{\text{imp}} \gtrsim E_{\text{roll}}$, internal restructuring occurs through inelastic rolling among constituent monomers (Dominik & Tielens 1997; see also Figure 1(c)). In this case, the final volume V_{1+2} depends on E_{imp} as well as on V_1 and V_2 .

For hit-and-stick collisions ($E_{\text{imp}}/E_{\text{roll}} \rightarrow 0$), Okuzumi et al. (2009) obtained an empirical formula for V_{1+2} ,

$$V_{1+2} = V_{1+2,HS} \equiv V_1 + V_2 + V_{\text{void}}, \quad (10)$$

where V_1 and V_2 ($\leq V_1$) are the volumes of the two colliding aggregates, and

$$V_{\text{void}} = \min \left\{ 0.99 - 1.03 \ln \left(\frac{2}{V_1/V_2 + 1} \right), 6.94 \right\} V_2 \quad (11)$$

is the volume of the voids created in the collision (see Figure 1(b)). For $V_1 \approx V_2$, the void volume is approximately equal to V_1 , and hence the volume of the new aggregate is approximately given by $V_{1+2} \approx 3V_1$. This is equivalent to a fractal relation $V \propto m^{3/d_f}$, where $d_f \approx 2$ (see Section 4.2.1 of Okuzumi et al. 2009).

In the limit of $E_{\text{imp}} \gg E_{\text{roll}}$ and for head-on collision of equal-sized aggregates ($V_1 = V_2$), Suyama et al. (2008) showed that V_{1+2} obeys the relation

$$E_{\text{imp}} = - \int_{2^{6/5}V_1}^{V_{1+2}} P(V) dV. \quad (12)$$

Here, $P \equiv -dE_{\text{imp}}/dV$ is the dynamic compression strength of the merged aggregate given by (Wada et al. 2008)

$$P(V) = 2 \left(\frac{5}{3} \right)^6 \frac{b E_{\text{roll}}}{V_0} \left(\frac{\rho_{\text{int}}(V)}{\rho_0} \right)^{13/3} N_{1+2}^{2/3}, \quad (13)$$

where $b = 0.15$ is a dimensionless fitting parameter, $V_0 = m_0/\rho_0 = (4\pi/3)a_0^3$ is the monomer volume, $N_{1+2} = 2m_1/m_0$ is the number of monomers contained in the merged aggregate, and $\rho_{\text{int}} = 2m_1/V$ is the internal density of the merged aggregate. If we substitute Equation (13) into Equation (12), we obtain the equation that explicitly gives V_{1+2} as a function of E_{roll} and V_1 ,

$$V_{1+2} = \left[\frac{(3/5)^5 E_{\text{imp}}}{N_{1+2}^5 b E_{\text{roll}} V_0^{10/3}} + \left(2V_1^{5/6} \right)^{-4} \right]^{-3/10}. \quad (14)$$

This equation basically expresses the energy balance in collisional compression, but some caution is needed in interpreting it. First, the initial state for the compression is chosen to be $V = 2^{6/5}V_1$, although the volume just after contact is $V = 3V_1$ (see above). This is based on the fact that compaction from $V = 3V_1$ to $V = 2^{6/5}V_1$ occurs through partial compression of the new voids, which requires little energy (Suyama et al. 2008). Second, the dynamic compression strength P depends on mass N_{1+2} as well as on internal density ρ_{int} , meaning that P is not an intensive variable. This is due to the fact that dynamically compressed parts in the merged aggregate have a fractal structure with the fractal dimension of 2.5 (Wada et al. 2008). In fact, Equations (12)–(14) are more naturally described in terms of variables in the 2.5-dimensional space, $V_f \propto a^{5/2}$, $\rho_f \propto N_{1+2}/V_f$, and $P_f = -dE_{\text{imp}}/dV_f$ (see Wada et al. 2008; Suyama et al. 2008). An important point here is that aggregates become stronger and stronger against dynamic compression as they grow because of the $N_{1+2}^{2/3}$ factor in P .

Equations (10) and (14) express how the volume of the merged aggregate is determined in the limits of $E_{\text{imp}} \ll E_{\text{roll}}$ and $E_{\text{imp}} \gg E_{\text{roll}}$, respectively. To properly take into account intermediate cases ($E_{\text{imp}} \sim E_{\text{roll}}$), we adopt an updated analytic formula given recently by Suyama et al. (2012). This reads

$$V_{1+2} = \begin{cases} \left[\left(1 - \frac{E_{\text{imp}}}{3bE_{\text{roll}}} \right) V_{1+2,\text{HS}}^{5/6} + \frac{E_{\text{imp}}}{3bE_{\text{roll}}} (V_1^{5/6} + V_2^{5/6}) \right]^{6/5} & \text{(if } V_{1+2,\text{HS}}^{5/6} > V_1^{5/6} + V_2^{5/6} \text{ and } E_{\text{imp}} < 3bE_{\text{roll}}), \\ \left[\frac{(3/5)^5 (E_{\text{imp}} - 3bE_{\text{roll}})}{N_{1+2}^5 b E_{\text{roll}} V_0^{10/3}} + (V_1^{5/6} + V_2^{5/6})^{-4} \right]^{-3/10} & \text{(if } V_{1+2,\text{HS}}^{5/6} > V_1^{5/6} + V_2^{5/6} \text{ and } E_{\text{imp}} > 3bE_{\text{roll}}), \\ \left[\frac{(3/5)^5 E_{\text{imp}}}{N_{1+2}^5 b E_{\text{roll}} V_0^{10/3}} + V_{1+2,\text{HS}}^{-10/3} \right]^{-3/10} & \text{(if } V_{1+2,\text{HS}}^{5/6} < V_1^{5/6} + V_2^{5/6}), \end{cases} \quad (15)$$

where N_{1+2} is now defined as $(m_1 + m_2)/m_0$. Note that this equation reduces to Equations (10) when $E_{\text{imp}} \ll E_{\text{roll}}$, and to Equation (14) when $V_1 = V_2$ and $E_{\text{imp}} \gg E_{\text{roll}}$. Suyama et al. (2012) derived Equation (15) by taking into account small energy loss in the partial compression of the new voids. In addition, unlike Equation (14), Equation (15) takes into account the cases where colliding aggregates have different volumes and masses ($V_1 \neq V_2$, $m_1 \neq m_2$). Suyama et al. (2012) confirmed that Equation (15) reproduces the results of numerical collision experiments within an error of 20% as long as the mass ratio $m_2/m_1 (\leq 1)$ between the colliding aggregates is larger than 1/16.

We comment on three important caveats regarding our porosity recipe. First, Equation (15) is still untested for cases where colliding aggregates have very different sizes ($m_2/m_1 < 1/16$). Therefore, the validity of using Equation (15) is at present only guaranteed for the case where “similar-sized” ($m_2/m_1 \gtrsim 1/16$) collisions dominate the growth of aggregates. We will carefully check this validity in Section 3.2. Second, Equation (15) ignores offset collisions, in which a considerable fraction of the impact energy is spent for stretching rather than compaction (Wada et al. 2007; Paszun & Dominik 2009). For this reason, Equation (15) underestimates the porosity increase upon collision. Third, we do not consider non-collisional compression (e.g., static compression due to gas drag forces), which could contribute to the compaction of very large aggregates. We will discuss the second and third points in more detail in Section 5.4.

In addition to V , we need to know the projected area A of aggregates to calculate the stopping time t_s . Unfortunately, a naive relation $A = \pi a^2$ breaks down when the fractal dimension of the aggregate is less than 2, since πa^2 increases faster than mass for this case while A does not. A projected area growing faster than mass means a coupling to the gas becoming stronger and stronger as the aggregate grows, which is clearly unrealistic. To avoid this, we use an empirical formula by Okuzumi et al. (2009) that well reproduces the mean projected area \bar{A} of aggregates with monomer number $N = m/m_0$ and radius a for both fractal and compact aggregates. With this formula, all aggregates in our simulations are guaranteed to decouple from the gas as they grow. We remark that this treatment is only relevant to fractal aggregates with $d_f \lesssim 2$; for more compact aggregates, the empirical formula reduces to the usual relation $A \approx \pi a^2$.

The rolling energy E_{roll} has not been measured so far for submicron-sized icy particles, but can be estimated in the following way. It is anticipated by microscopic friction theory (Dominik & Tielens 1995) that the critical rolling force $F_{\text{roll}} \equiv E_{\text{roll}}/(\pi a_0/2)$ is a material constant (i.e., E_{roll} is proportional to the monomer radius a_0). Recently, a rolling force of $F_{\text{roll}} = (1.15 \pm 0.24) \times 10^{-3}$ dyn has been measured for micron-sized ice particles (Gundlach et al. 2011). Given that F_{roll} is independent of a_0 , the measured force implies the rolling energy of $E_{\text{roll}} = (\pi a_0/2) F_{\text{roll}} \approx 1.8 \times 10^{-8}$ erg for $a_0 = 0.1 \mu\text{m}$. We use this value in our simulations.

2.3.2. Collision Velocity

We consider Brownian motion, radial and azimuthal drift, vertical settling, and turbulence as sources of the collision velocity, and give the collision velocity Δv as the root sum square of these contributions,

$$\Delta v = \sqrt{(\Delta v_B)^2 + (\Delta v_r)^2 + (\Delta v_\phi)^2 + (\Delta v_z)^2 + (\Delta v_t)^2}, \quad (16)$$

where Δv_B , Δv_r , Δv_ϕ , Δv_z , and Δv_t are the relative velocities induced by Brownian motion, radial drift, azimuthal drift, vertical settling, and turbulence, respectively.

The Brownian-motion-induced velocity is given by

$$\Delta v_B = \sqrt{\frac{\pi m_1 m_2}{8(m_1 + m_2)k_B T}}, \quad (17)$$

where m_1 and m_2 are the masses of the two colliding aggregates.

The relative velocity due to radial drift is given by $\Delta v_r = |v_r(t_{s,1}) - v_r(t_{s,2})|$, where $t_{s,1}$ and $t_{s,2}$ are the stopping times of the colliding aggregates, and v_r is the radial velocity given by Equation (6). Similarly, the relative velocity due to differential azimuthal motion is given by $\Delta v_\phi = |v'_\phi(t_{s,1}) - v'_\phi(t_{s,2})|$, where

$$v'_\phi = -\frac{\eta v_K}{1 + (\Omega t_s)^2} \quad (18)$$

is the deviation of the azimuthal velocity from the local Kepler velocity (Adachi et al. 1976; Weidenschilling 1977; Nakagawa et al. 1986). Here, we have neglected the back-reaction from dust to gas as we already did for the radial velocity (see Sections 2.3.2 and 5.2.1).

For the differential settling velocity, we assume $\Delta v_z = |v_z(t_{s,1}) - v_z(t_{s,2})|$, where

$$v_z = -\frac{\Omega^2 t_s z}{1 + \Omega t_s}. \quad (19)$$

Equation (19) reduces to the terminal settling velocity $v_z = -\Omega^2 t_s z$ in the strong coupling limit $\Omega t_s \ll 1$, and to the amplitude of the vertical oscillation velocity at $\Omega t_s \gg 1$ (Brauer et al. 2008a).

For the turbulence-driven relative velocity, we use an analytic formula for Kolmogorov turbulence derived by Ormel & Cuzzi (2007, their Equation (16)). This analytic formula has three limiting expressions (Equations (27)–(29) of Ormel & Cuzzi 2007):

$$\Delta v_t \approx \begin{cases} \delta v_g \text{Re}_t^{1/4} \Omega |t_{s,1} - t_{s,2}|, & t_{s,1} \ll t_\eta, \\ (1.4 \dots 1.7) \times \delta v_g \sqrt{\Omega t_{s,1}}, & t_\eta \ll t_{s,1} \ll \Omega^{-1}, \\ \delta v_g \left(\frac{1}{1 + \Omega t_{s,1}} + \frac{1}{1 + \Omega t_{s,2}} \right)^{1/2}, & \Omega t_{s,1} \gg 1, \end{cases} \quad (20)$$

where Re_t is the turbulent Reynolds number, $t_\eta = \text{Re}_t^{-1/2} t_L$ is the turnover time of the smallest eddies, and the numerical prefactor (1.4...1.7) in the second equality depends on the ratio between the stopping times, $t_{s,2}/t_{s,1}$. The turbulent Reynolds number is given by $\text{Re}_t = D_g/\nu_{\text{mol}}$, where $\nu_{\text{mol}} = v_{\text{th}} \lambda_{\text{mfp}}/2$ is the molecular viscosity. For $t_{s,1} \sim t_{s,2}$, the maximum induced velocity is $\Delta v_t \approx \delta v_g$, which is reached when $\Omega t_{s,1} \approx 1$.

When two colliding aggregates belong to the Epstein regime and their stopping times are much shorter than t_η ($\ll \Omega^{-1}$), the relative velocity driven by sedimentation and turbulence is approximately proportional to the difference between the mass-to-area ratios m/A of two colliding aggregates. In this case, as pointed out by Okuzumi et al. (2011a), the dispersion of the mass-to-area ratio becomes important for fractal aggregates of $d_f \lesssim 2$, since the mean mass-to-area ratio of the aggregates approaches to a constant and hence the difference in $m/\bar{A}(m)$ vanishes. To take into account the dispersion effect, we evaluate the differential mass-to-area ratio as

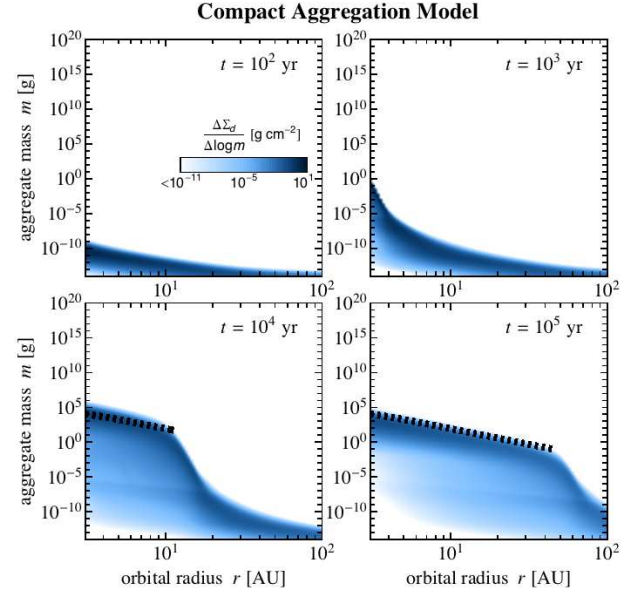


Figure 2. Aggregate size distribution $\Delta \Sigma_d / \Delta \log m$ at different times t for the compact aggregation model ($\rho_{\text{int}} = 1.4 \text{ g cm}^{-3}$) as a function of orbital radius r and aggregate mass m . The dotted lines mark the aggregate size at which Ωt_s exceeds 0.1.

$[\Delta(m/A)]^2 = [m_1/\bar{A}_1 - m_2/\bar{A}_2]^2 + \epsilon^2[(m_1/\bar{A}_1)^2 + (m_2/\bar{A}_2)^2]$, where $\bar{A}_j = \bar{A}(m_j)$ ($j = 1, 2$) are the mean projected area of aggregates with mass m_j (see Section 2.3.1) and ϵ is the standard deviation of the mass-to-area ratio divided by the mean (for the derivation, see the Appendix of Okuzumi et al. 2011a). We assume $\epsilon = 0.1$ in accordance with the numerical estimate by Okuzumi et al. (2011a).

2.4. Numerical Method

We solve Equations (1) and (8) numerically with an explicit time-integration scheme and a fixed-bin method. The radial domain is taken to be outside the snow line, $3 \text{ AU} \leq r \leq 150 \text{ AU}$, discretized into 100 rings with an equal logarithmic width $\Delta \ln(r[\text{AU}]) = (\ln 150 - \ln 3)/100$. The advection terms are calculated by the spatially first-order upwind scheme. We impose the outflow and zero-flux boundary conditions at the innermost and outermost radii ($r = 3 \text{ AU}$ and 150 AU), respectively; thus, the total dust mass inside the domain is a decreasing function of time. Our numerical results are unaffected by the choice of the boundary condition at the outermost radius, since dust growth at this location is too slow to cause appreciable radial drift within the calculated time. The coagulation terms are calculated by the method given by Okuzumi et al. (2009). Specifically, at the center of each radial ring we divide the mass coordinate into linearly spaced bins $m_k = km_0$ ($k = 1, 2, \dots, N_{bd}$) for $m \leq N_{bd}m_0$ and logarithmically spaced bins $m_k = m_{k-1}10^{1/N_{bd}}$ ($k = N_{bd} + 1, \dots$) for $m > N_{bd}m_0$, where N_{bd} is an integer. We adopt $N_{bd} = 40$; as shown by Okuzumi et al. (2009), the calculation results well converge as long as $N_{bd} \geq 40$. The time increment Δt is adjusted at every time step so that the fractional decreases in N and VN fall below 0.5 (i.e., $\Delta t < -0.5(\partial \ln N / \partial t)^{-1}$ and $\Delta t < -0.5(\partial \ln VN / \partial t)^{-1}$) at all bins.

3. RESULTS

3.1. Compact Aggregation

To begin with, we show the result of compact aggregation. In this simulation, we fixed the internal density $\rho_{\text{int}} \equiv m/V$ of

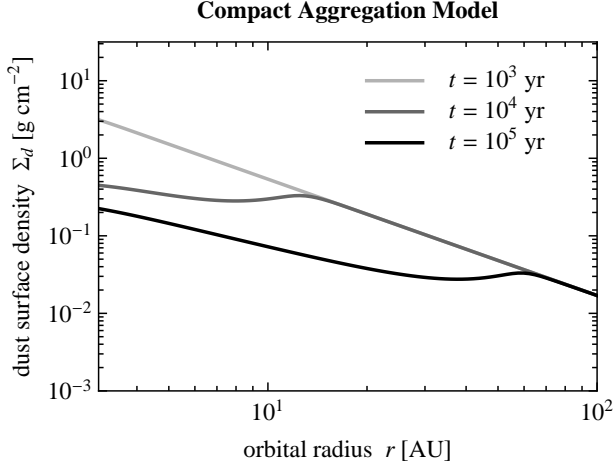


Figure 3. Radial profiles of the total dust surface density Σ_d at different times for the compact aggregation model ($\rho_{\text{int}} = 1.4 \text{ g cm}^{-3}$).

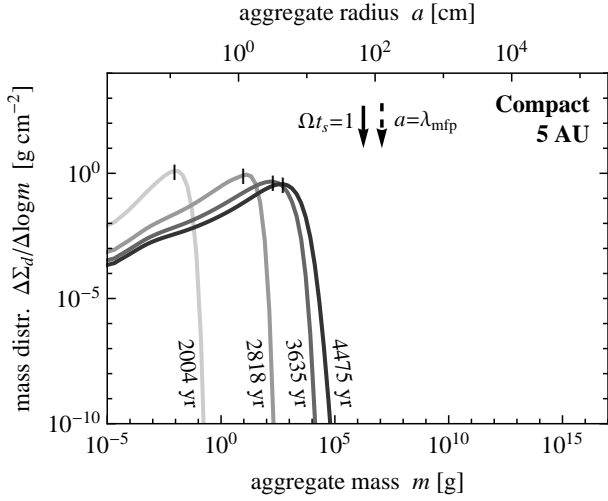


Figure 4. Aggregate size distribution $\Delta\Sigma_d/\Delta\log m$ at $r = 5 \text{ AU}$ and $t = 2000 \text{ yr}$ – 4470 yr for the compact aggregation model. The dashed and solid arrows indicate the aggregate sizes at which $a = \lambda_{\text{mfp}}$ and $\Omega_{t_s} = 1$, respectively. Shown at the top of the panel is the aggregate radius a . The vertical bars indicate the weighted average mass $\langle m \rangle_m$ (Equation (21)).

the aggregates to the material density $\rho_0 = 1.4 \text{ g cm}^{-3}$, and solved only the evolutionary equation for the radial size distribution $N(r, m)$ (Equation (1)), as done in previous studies (e.g., Brauer et al. 2008a). Figure 2 shows the snapshots of the radial size distribution at different times. Here, the distribution is represented by the dust surface density per decade of aggregate mass, $\Delta\Sigma_d/\Delta\log m \equiv \ln(10)m^2 N(r, m)$. At each orbital radius, dust growth proceeds without significant radial drift until the stopping time of the aggregates reaches $\Omega_{t_s} \sim 0.1$ (the dotted lines in Figure 2). However, as the aggregates grow, the radial drift becomes faster and faster, and further growth becomes limited only along the line $\Omega_{t_s} \sim 0.1$ on the r – m plane. Figure 3 shows the evolution of the total dust surface density $\Sigma_d \equiv \int m N dm = \int (\Delta\Sigma_d/\Delta\log m) d\log m$. We see that a significant amount of dust has been lost from the planet-forming region $r \lesssim 30 \text{ AU}$ within 10^5 yr . In this region, the dust surface density scales as r^{-1} ,⁴ and hence the

⁴ It can be analytically shown (Birnstiel et al. 2012) that the dust surface density profile obeys a scaling $\Sigma_d \propto \sqrt{\Sigma_g/(r^2\Omega)}$ ($\propto r^{-1}$ for $\Sigma_g \propto r^{-3/2}$) when

dust-to-gas surface density ratio $\propto r^{-1}/\Sigma_g \propto r^{1/2}$ decreases toward the central star.

Figure 4 shows the evolution of the dust size distribution observed at $r = 5 \text{ AU}$. Here, in order to characterize the typical aggregate size at each evolutionary stage, we introduce the weighted average mass $\langle m \rangle_m$ defined by

$$\langle m \rangle_m \equiv \frac{\int m^2 N dm}{\int m N dm} = \frac{1}{\Sigma_d} \int m \frac{\Delta\Sigma_d}{\Delta\log m} d\log m. \quad (21)$$

The weighted average mass approximately corresponds to the aggregate mass at the peak of $\Delta\Sigma_d/\Delta\log m$ (see, e.g., Ormel et al. 2007; Okuzumi et al. 2011a). In Figure 4, the weighted average mass at each time is indicated by the short vertical line. At $r = 5 \text{ AU}$, the growth–drift equilibrium is reached at $t \approx 4000 \text{ yr}$, and the typical size of the aggregates is $\langle m \rangle_m \approx 500 \text{ g}$ in mass ($\approx 4 \text{ cm}$ in radius, $\approx 0.07\Omega^{-1}$ in stopping time). Note that the final aggregate radius is much smaller than the mean free path λ_{mfp} of gas molecules (the dashed arrow in Figure 4), which means that the gas drag onto the aggregates is determined by Epstein’s law. As we will see in the following, porosity evolution allows aggregates to reach the Stokes drag regime at much smaller Ω_{t_s} .

3.2. Porous Aggregation

Now we show how porosity evolution affects dust evolution. Here, we solve the evolutionary equation for $V(r, m)$ (Equation (8)) simultaneously with that for $N(r, m)$ (Equation (1)). The result is shown in Figure 5, which displays the snapshots of the aggregate size distribution $\Delta\Sigma_d/\Delta\log m$ and internal density $\rho_{\text{int}} = m/V$ at different times t as a function of r and m . The evolution of the total dust surface density Σ_d is shown in Figure 6.

The left four panels of Figure 5 show how the radial size distribution evolves in the porous aggregation. At $t < 10^3 \text{ yr}$, the evolution is qualitatively similar to that in compact aggregation (Section 3.1). However, in later stages, the evolution is significantly different. We observe that aggregates in the inner region of the disk ($r < 10 \text{ AU}$) undergo rapid growth and eventually overcome the radial drift barrier lying at $\Omega_{t_s} \sim 1$ (dashed lines in Figure 5) within $t \sim 10^4 \text{ yr}$. At this stage, the radial profile of the total dust surface density Σ_d is hardly changed from the initial profile, as is seen in Figure 6. In the outer region ($r > 10 \text{ AU}$), aggregates do drift inward before they reach $\Omega_{t_s} \sim 1$ as in the compact aggregation model. However, unlike in the compact aggregation, the inward drift results in the pileup of dust materials in the inner region ($r \approx 4$ – 9 AU) rather than the loss of them from outside the snow line (see Figure 6). This occurs because most of the drifting aggregates get captured by aggregates that have already overcome the drift barrier. As a result of this, the dust-to-gas mass ratio in the inner regions is enhanced by a factor of several in 10^5 yr .

The right four panels of Figure 5 show the evolution of the internal density $\rho_{\text{int}} = m/V$ as a function of r and m . First thing to note is that the dust particles grow into low-density objects at every location until their internal density reaches $\rho_{\text{int}} \sim 10^{-5}$ – $10^{-3} \text{ g cm}^{-3}$. In this stage, the internal density decreases as $\rho_{\text{int}} \approx (m/m_0)^{-1/2}\rho_0$, meaning that the dust particles grow into fractal aggregates with the fractal dimension $d_f \approx 2$ (Okuzumi et al. 2009). The fractal growth generally occurs in early growth stages where the impact energy

radial drift balances with turbulence-driven growth.

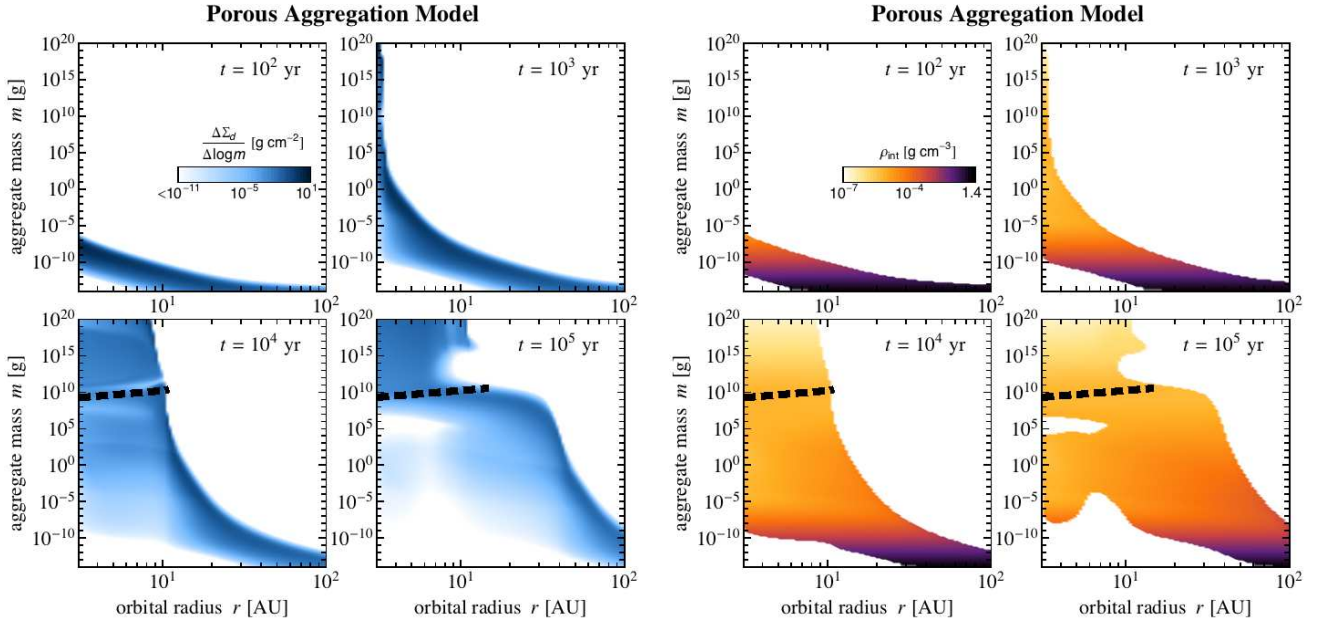


Figure 5. Aggregate size distribution $\Delta\Sigma_d/\Delta\log m$ (left four panels) and internal density $\rho_{\text{int}} = m/V$ (right four panels) at different times t for the porous aggregation model as a function of orbital radius r and aggregate mass m . The dashed lines mark the aggregate size at which Ωt_s exceeds unity.

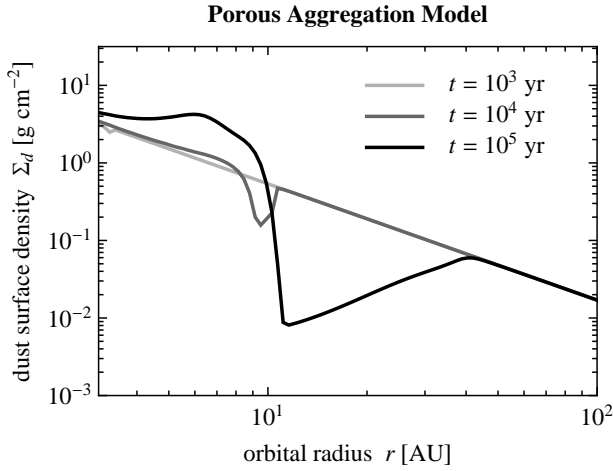


Figure 6. Radial profiles of the total dust surface density Σ_d at different times for the porous aggregation model.

is too low to cause collisional compression, i.e., $E_{\text{imp}} \ll E_{\text{roll}}$ (e.g., Blum 2004; Ormel et al. 2007; Zsom et al. 2010). At $m \sim 10^{-4}$ – 10^{-6} g, the fractal growth stage terminates, followed by the stage where collisional compression becomes effective ($E_{\text{imp}} \gg E_{\text{roll}}$). In this late stage, the internal density decreases more slowly or is kept at a constant value depending on the orbital radius. We will examine the density evolution in more detail in Section 3.2.2.

Figure 7 shows the evolution of the mass distribution function at $r = 5$ AU during $t \approx 1200$ – 2500 yr. The evolution of the weighted average mass $\langle m \rangle_m$ is shown in Figure 8. It is seen that the acceleration of the growth begins when the aggregate size a exceeds the mean free path of gas molecules, λ_{mfp} (the dashed arrow in Figure 7). This suggests that the acceleration is due to the change in the aerodynamical property of the aggregates. At $a \approx \lambda_{\text{mfp}}$, the gas drag onto the aggregates begins to obey Stokes' law. In the Stokes regime, the stopping time t_s of aggregates quickly increases with size (see Section 2.2). This causes the quick growth of the aggre-

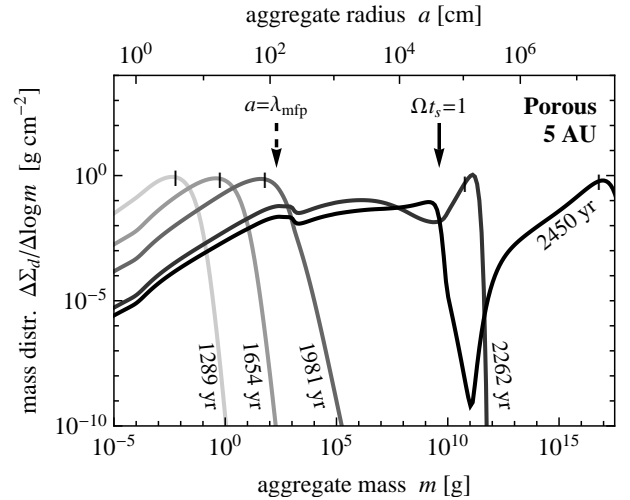


Figure 7. Aggregate mass distribution $\Delta\Sigma_d/\Delta\log m$ at $r = 5$ AU and $t = 1289$ yr– 2450 yr for the porous aggregation model. The dashed and solid arrows indicate the sizes at which $a = \lambda_{\text{mfp}}$ and $\Omega t_s = 1$, respectively. Shown at the top of the panel is the aggregate radius a measured at $t = 2450$ yr. The vertical bars indicate the weighted average mass $\langle m \rangle_m$ (Equation (21)).

gates since the relative velocity between aggregates increases with t_s (as long as $\Omega t_s < 1$). As a result of the growth acceleration, the aggregates grow from $a \approx \lambda_{\text{mfp}}$ to $\Omega t_s \approx 1$ within 300 yr, which is short enough for them to break through the radial drift barrier.

The decrease in the internal density plays an important role on the growth acceleration. More precisely, the low internal density allows the aggregates to reach $a \approx \lambda_{\text{mfp}}$ at early growth stages, i.e., at small Ωt_s . In fact, the growth acceleration was not observed in the compact aggregation, since the aggregate size is smaller than the mean free path at *all* $\Omega t_s < 1$ (see Figure 4). A more rigorous explanation for this will be given in Section 4.

3.2.1. Projectile Mass Distribution

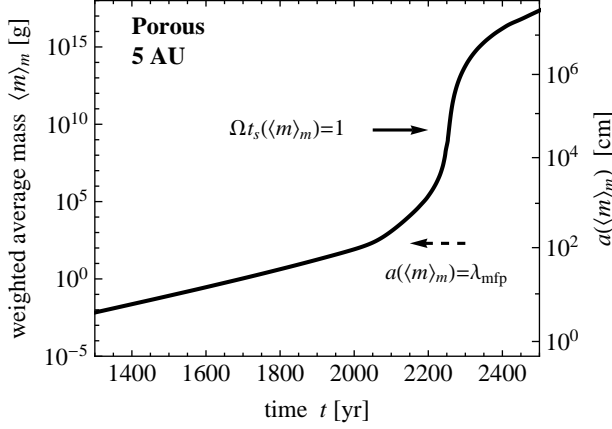


Figure 8. Weighted average mass $\langle m \rangle_m$ (Equation (21)) at $r = 5$ AU as a function of time t for the porous aggregation model. Shown at the right of the panel is the corresponding aggregate radius $a(\langle m \rangle_m)$. The dashed and solid arrows indicate the sizes at which $a(\langle m \rangle_m) = \lambda_{\text{mfp}}$ and $\Omega t_s(\langle m \rangle_m) = 1$, respectively.

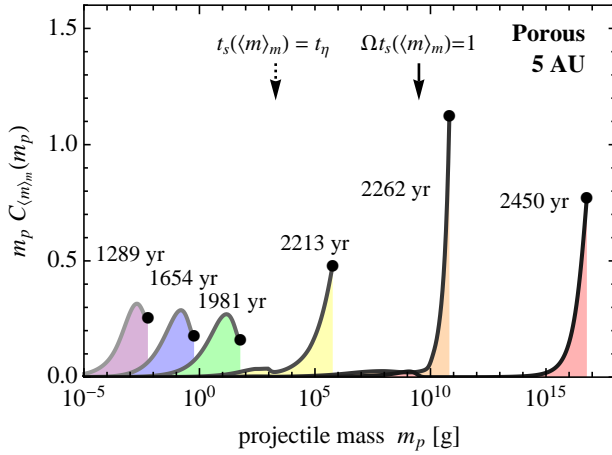


Figure 9. Normalized projectile mass distribution per unit logarithmic projectile mass, $m_p C_{m_i}(m_p)$, for a target with mass $m_t = \langle m \rangle_m$ at different times t (1289 yr–2450 yr) at $r = 5$ AU for the porous aggregation model (see Equation (22) for the definition of $C_{m_i}(m_p)$). The filled circles show the values for equal-sized collisions, $m_p = m_t (= \langle m \rangle_m)$. The dotted and solid arrows indicate the target mass at which $t_s = t_\eta$ and $\Omega t_s = 1$, respectively.

As noted in Section 2.3.1, our porosity change model has only been tested for collisions between similar-sized aggregates. To check the validity of using this model, we introduce the projectile mass distribution function (Okuzumi et al. 2009):

$$C_{m_i}(m_p) \equiv \frac{m_p K(m_p, m_i) N(m_p)}{\int_0^{m_i} m'_p K(m'_p, m_i) N(m'_p) dm'_p}, \quad m_p \leq m_i, \quad (22)$$

which is normalized so that $\int_0^{m_i} C_{m_i}(m_p) dm_p = 1$. The denominator of $C_{m_i}(m_p)$ is equal to the growth rate $t_{\text{grow}}^{-1} \equiv d \ln m_i / dt$ of a target having mass m_i (see Okuzumi et al. 2009). Hence, the quantity $C_{m_i}(m_p) dm_p$ measures the contribution of projectiles within mass range $[m_p, m_p + dm_p]$ to the growth of the target.

Figure 9 shows the projectile mass distribution per unit $\ln m_p$, $m_p C_{m_i}(m_p)$, for targets with mass $m_t = \langle m \rangle_m$ at $r = 5$ AU and at different t . We see that the growth of the $m_t = \langle m \rangle_m$ target is dominated by projectiles within a mass

range $0.1 m_t \leq m_p \leq m_t$. In fact, the projectile mass distribution integrated over $0.1 m_t \leq m_p \leq m_t$ exceeds 50% for all the cases presented in Figure 9. This means that the growth of aggregates is indeed dominated by collisions with similar-sized ones as required by the limitation of our porosity model. This is basically the consequence of the fact that the aggregate mass distribution $\Delta \Sigma_d / \Delta \log m$ is peaked around the target mass $m \sim \langle m \rangle_m$ (see Figure 7). The mass ratio m_p / m_t at the peak of $m_p C_{m_i}(m_p)$ reflects the size dependence of the turbulence-driven relative velocity Δv_t , which is the main source of the collision velocity in our simulation. At $t \leq 2000$ yr ($\langle m \rangle_m \leq 10^3$ g), the dominant projectile mass is lower than $m_t (= \langle m \rangle_m)$, since both the target and projectiles are tightly coupled to turbulence (i.e., $t_s(m_t), t_s(m_p) < t_\eta$) and hence Δv_t vanishes at equal-sized collisions (see the first expression of Equation (20)). At $t \gtrsim 2000$ yr ($\langle m \rangle_m \gtrsim 10^3$ g), the target decouples from small turbulent eddies ($t_s(m_t) > t_\eta$). This results in the shift of the dominant collision mode to $m_p \approx m_t$ because Δv_t no more vanishes at equal-sized collisions (see the second line of Equation (20)).

3.2.2. Density Evolution History

To see the density evolution history in detail, we plot in Figure 10 the temporal evolution of the weighted average mass $\langle m \rangle_m$ and the internal density of aggregates with mass $m = \langle m \rangle_m$ at orbital radii $r = 5$ AU and 20 AU.

As mentioned above, dust particles initially grow into fractal aggregates of $d_f \approx 2$ until the impact energy E_{imp} becomes comparable to the rolling energy E_{roll} . With this fact, one can analytically estimate the aggregate size at which the fractal growth terminates. Our simulation shows that the collision velocity between the fractal aggregates is approximately given by the turbulence-driven velocity in the strong-coupling limit (Equation (20) with $t_s \ll t_\eta$). Assuming that the collisions mainly occur between aggregates of similar sizes (see Section 3.2.1), the reduced mass and the collision velocity are roughly given by $m/2$ and $\delta v_g \text{Re}_t^{1/4} \Omega t_s$, respectively. In addition, we use the fact that fractal aggregates with $d_f \approx 2$ have the mass-to-area ratio comparable to their constituent monomers. This means that the stopping time of the aggregates is as short as the monomers and is hence given by Epstein's law. Thus, the impact energy is approximated as

$$E_{\text{imp}} \approx \frac{m}{4} \Delta v_t^2 \approx \frac{3}{8} m \left(\frac{\delta v_g \text{Re}_t^{1/4} \Omega}{\rho_g v_{\text{th}}} \right)^2 \left(\frac{3m}{4A} \right)^2. \quad (23)$$

Furthermore, using the definitions for ρ_g , v_{th} , and Re_t , we have $\rho_g v_{\text{th}} = (2/\pi) \Sigma_g \Omega$ and $\text{Re}_t = \alpha_D \Sigma_g \sigma_{\text{mol}} / (2m_g)$ for the midplane. Substituting them into Equation (23) and using $\delta v_g = \sqrt{\alpha_D} c_s$ and $m/A \approx m_0 / (\pi a_0^2) = 4 \rho_0 a_0 / 3$, we obtain

$$E_{\text{imp}} \approx \frac{3\pi^2}{32\sqrt{2}} \alpha_D^{3/2} m c_s^2 \left(\frac{\Sigma_g \sigma_{\text{mol}}}{m_g} \right)^{1/2} \left(\frac{\rho_0 a_0}{\Sigma_g} \right)^2. \quad (24)$$

Thus, the impact energy is proportional to the mass. We define the rolling mass m_{roll} by the condition $E_{\text{imp}} = E_{\text{roll}}$. Using Equation (24), the rolling mass is evaluated as

$$m_{\text{roll}} \approx \frac{32\sqrt{2}}{3\pi^2} \frac{E_{\text{roll}}}{c_s^2 \alpha_D^{3/2}} \left(\frac{m_g}{\Sigma_g \sigma_{\text{mol}}} \right)^{1/2} \left(\frac{\Sigma_g}{\rho_0 a_0} \right)^2 \\ \sim 10^{-4} \text{ g} \left(\frac{\alpha_D}{10^{-3}} \right)^{-3/2} \left(\frac{T}{100 \text{ K}} \right)^{-1} \left(\frac{\Sigma_g}{100 \text{ g cm}^{-2}} \right)^{3/2}$$

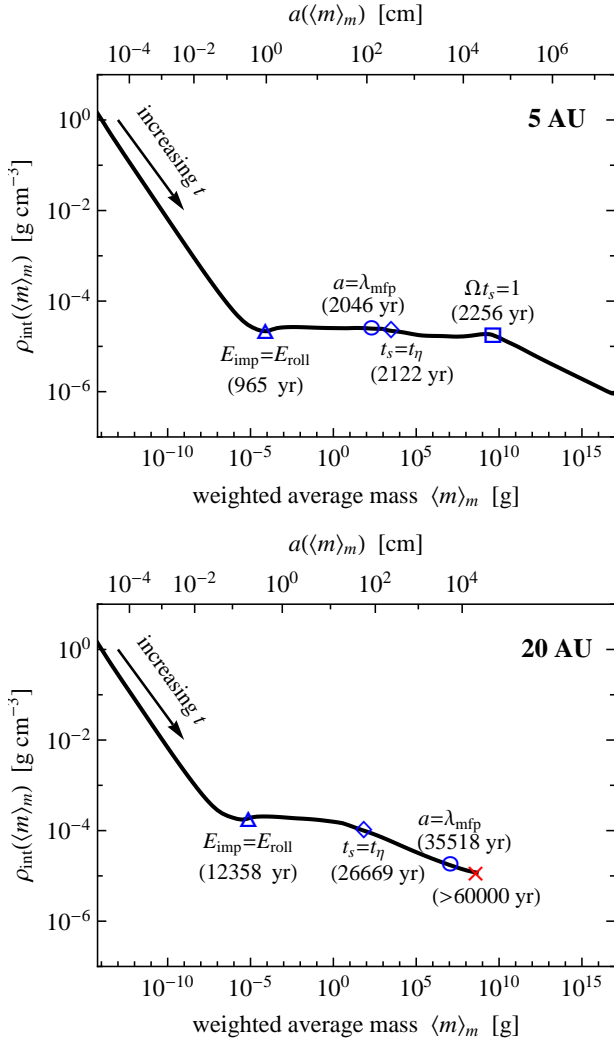


Figure 10. Temporal evolution of the weighted average mass $\langle m \rangle_m$ and the internal density $\rho_{\text{int}}(\langle m \rangle_m)$ at orbital radii $r = 5$ AU (upper panel) and 20 AU (lower panel). Shown at the top of the panels is the aggregate radius $a(\langle m \rangle_m)$ at each orbital radius. The triangles, circles, diamonds, and square mark the sizes at which $E_{\text{imp}} = E_{\text{roll}}$, $a = \lambda_{\text{mfp}}$, $t_s = t_\eta$, and $\Omega t_s = 1$, respectively. At $r = 20$ AU, dust growth stalls due to the radial drift barrier (cross symbol) before reaching $\Omega t_s = 1$.

$$\times \left(\frac{F_{\text{roll}}}{10^{-3} \text{ dyn}} \right) \left(\frac{\rho_0}{1 \text{ g cm}^{-3}} \right)^{-2} \left(\frac{a_0}{0.1 \mu\text{m}} \right)^{-1}, \quad (25)$$

where we have used that $E_{\text{roll}} = (\pi a_0/2) F_{\text{roll}}$ (see Section 2.3.1). Using the relations $a \approx (m/m_0)^{1/2} a_0$ and $\rho_{\text{int}} \approx (m/m_0)^{-1/2} \rho_0$ for $d_f \approx 2$ aggregates, the corresponding radius and internal density are found to be

$$a_{\text{roll}} \sim 1 \text{ cm} \left(\frac{m_{\text{roll}}}{10^{-4} \text{ g}} \right)^{1/2}, \quad (26)$$

$$\rho_{\text{int,roll}} \sim 10^{-5} \text{ g cm}^{-3} \left(\frac{m_{\text{roll}}}{10^{-4} \text{ g}} \right)^{-1/2}. \quad (27)$$

The triangles in Figure 10 mark the rolling mass at $r = 5$ AU and 20 AU predicted by Equation (25). The analytic prediction well explains when the decrease in ρ_{int} terminates.

The density evolution is more complicated at $m > m_{\text{roll}}$, where collisional compression is no longer negligible (i.e., $E_{\text{imp}} > E_{\text{roll}}$). At $r = 5$ AU, the internal density is approx-

imately constant until the stopping time reaches $\Omega t_s = 1$, and then decreases as $\rho_{\text{int}} \propto m^{-1/5}$. At $r = 20$ AU, by contrast, the density is kept nearly constant until $m \sim 10^2 \text{ g}$ ($a \sim 10^2 \text{ cm}$), and then decreases as $\rho_{\text{int}} \propto m^{-1/8}$.

As shown below, the density histories mentioned above can be directly derived from the porosity change recipe we adopted. Let us assume again that aggregates grow mainly through collisions with similar-sized ones ($m_1 \approx m_2$ and $V_1 \approx V_2$). In this case, the evolution of ρ_{int} at $E_{\text{imp}} \gg E_{\text{roll}}$ is approximately given by Equation (14). Furthermore, we neglect the term $(2V_1^{5/6})^{-4}$ in Equation (14) assuming that the impact energy is sufficiently large (which is true as long as $\Omega t_s < 1$; see below). Under these assumptions, the internal density of aggregates after collision, $\rho_{\text{int}} = 2m_1/V_{1+2}$, is approximately given by

$$\rho_{\text{int}} \approx \left(\frac{3}{5} \right)^{3/2} \left(\frac{E_{\text{imp}}}{N_{1+2} b E_{\text{roll}}} \right)^{3/10} N_{1+2}^{-1/5} \rho_0, \quad (28)$$

where $N_{1+2} = 2m_1/m_0$. Since the impact energy $E_{\text{imp}} \approx m_1(\Delta v)^2/4$ is proportional to $N_{1+2}(\Delta v)^2$, Equation (28) implies that

$$\rho_{\text{int}} \propto (\Delta v)^{3/5} m^{-1/5}, \quad (29)$$

where we have dropped the subscript for mass for clarity. Equation (29) gives the relation between ρ_{int} and m if we know how the impact velocity depends on them. Explicitly, if $\Delta v \propto m^\beta \rho_{\text{int}}^\gamma$, Equation (29) leads to

$$\rho_{\text{int}} \propto m^{(3\beta-1)/(5-3\gamma)}. \quad (30)$$

In our simulation, the main source of the relative velocity is turbulence. The turbulence-driven velocity depends on t_s as $\Delta v_t \propto t_s$ at $t_s \ll t_\eta$ and $\Delta v_t \propto \sqrt{t_s}$ at $t_\eta \ll t_s \ll t_L (= \Omega^{-1})$ (see Equation (20)). As found from Equation (4), the stopping time depends on ρ_{int} and m as $t_s \propto m/A \propto m/a^2 \propto m^{1/3} \rho_{\text{int}}^{2/3}$ in the Epstein regime ($a \ll \lambda_{\text{mfp}}$) and as $t_s \propto ma/A \propto m^{2/3} \rho_{\text{int}}^{1/3}$ in the Stokes regime ($a \gg \lambda_{\text{mfp}}$). Using these relations with Equation (30), we find four regimes for density evolution,

$$\rho_{\text{int}} \propto \begin{cases} m^0, & a \ll \lambda_{\text{mfp}} \text{ and } t_s \ll t_\eta, \\ m^{1/4}, & a \gg \lambda_{\text{mfp}} \text{ and } t_s \ll t_\eta, \\ m^{-1/8}, & a \ll \lambda_{\text{mfp}} \text{ and } t_\eta \ll t_s \ll t_L, \\ m^0, & a \gg \lambda_{\text{mfp}} \text{ and } t_\eta \ll t_s \ll t_L. \end{cases} \quad (31)$$

The circles, diamonds, and square in Figure 10 mark the size at which $a = \lambda_{\text{mfp}}$ (i.e., $t_s^{(\text{Ep})} \sim t_s^{(\text{St})}$), $t_s = t_\eta$, and $\Omega t_s = 1$, respectively. At $r = 5$ AU, the sizes at which $a = \lambda_{\text{mfp}}$ and $t_s = t_\eta$ nearly overlap, and hence only two velocity regimes $t_s = t_s^{(\text{Ep})} \ll t_\eta$ and $t_\eta \ll t_s = t_s^{(\text{St})} \ll t_L$ are effectively relevant. For both cases, Equation (31) predicts flat density evolution. At $r = 20$ AU, there is a stage in which $t_s \gg t_\eta$ and $a \ll \lambda_{\text{mfp}}$, for which Equation (31) predicts $\rho_{\text{int}} \propto m^{-1/8}$. These predictions are in agreement with what we see in Figure 10.

Equation (28) does not apply to the density evolution at $\Omega t_s > 1$, where the collision velocity no more increases and hence collisional compression becomes less and less efficient as the aggregates grow. However, if we go back to Equation (14) and assume that the impact energy E_{imp} is sufficiently small, we obtain $V_{1+2} \approx 2^{6/5} V_1$, or equivalently $V_{1+2}/m_{1+2}^{6/5} \approx V_1/m_1^{6/5}$, where $m_{1+2} = 2m_1$ is the aggregate mass after a collision. This implies that $V/m^{6/5}$ is kept constant during the growth, i.e., $V \propto m^{6/5}$, and hence we have

$\rho_{\text{int}} = m/V \propto m^{-1/5}$. This is consistent with the density evolution at $\Omega t_s > 1$ seen in the upper panel of Figure 10.

4. CONDITION FOR BREAKING THROUGH THE RADIAL DRIFT BARRIER

In this section, we explain why porous aggregates overcome the radial drift barrier in the inner region of the disk. We do this by comparing the timescale of aggregate growth and radial drift. We assume that dust aggregates grow mainly through collisions with similar-sized aggregates. As shown in Section 3.2.1, this is a good approximation for the growth of aggregates dominating the total mass of the system (i.e., aggregates with mass $m \sim \langle m \rangle_m$). The growth rate of the aggregate mass m at the midplane is then given by

$$\frac{dm}{dt} = \rho_d \sigma_{\text{coll}} \Delta v = \frac{\Sigma_d}{\sqrt{2\pi} h_d} A \Delta v, \quad (32)$$

where $\rho_d = \Sigma_d / (\sqrt{2\pi} h_d)$ is the spatial dust density at the midplane, and we have approximated σ_{coll} as the projected area A . Equation (32) can be rewritten in terms of the growth timescale as

$$t_{\text{grow}} \equiv \left(\frac{d \ln m}{dt} \right)^{-1} = \sqrt{2\pi} \frac{h_d}{\Delta v} \frac{m/A}{\Sigma_d} = \frac{4\sqrt{2\pi}}{3} \frac{h_d}{\Delta v} \frac{\rho_{\text{int}} a}{\Sigma_d}, \quad (33)$$

where we have used that $m = (4\pi/3) \rho_{\text{int}} a^3$ and $A = \pi a^2$. What we do here is to compare t_{grow} with the timescale for the radial drift given by

$$t_{\text{drift}} \equiv \left| \frac{d \ln r}{dt} \right|^{-1} = \frac{r}{|v_r|}. \quad (34)$$

Now we focus on the stage at which the radial drift velocity reaches the maximum value, i.e., $\Omega t_s = 1$. At this stage, the dust scale height is given by $h_d \approx (2\alpha_D/3)^{1/2} h_g$ according to Equation (3). In addition, we set $\Delta v \approx \sqrt{\alpha_D} c_s$ since the collision velocity between $\Omega t_s = 1$ particles is dominated by the turbulence-driven velocity. Using these relations and $h_g = c_s/\Omega$, we can rewrite Equation (33) as

$$t_{\text{grow}}|_{\Omega t_s=1} = \frac{4}{3} \sqrt{\frac{4\pi}{3}} \frac{(\rho_{\text{int}} a)_{\Omega t_s=1}}{\Sigma_d \Omega} \approx 40 \left(\frac{\Sigma_d / \Sigma_g}{0.01} \right)^{-1} \frac{(\rho_{\text{int}} a)_{\Omega t_s=1}}{\Sigma_g} t_K, \quad (35)$$

where $t_K = 2\pi/\Omega$ is the Keplerian orbital period. Thus, the growth timescale is shorter when the mass-to-area ratio $m/A \propto \rho_{\text{int}} a$ is smaller. Note that $t_{\text{grow}}|_{\Omega t_s=1}$ is independent of α_D since both h_d and Δv scale with $\sqrt{\alpha_D}$. By contrast, the drift timescale for $\Omega t_s = 1$ particles is

$$t_{\text{drift}}|_{\Omega t_s=1} = \frac{1}{\eta \Omega} \approx 40 \left(\frac{\eta}{4 \times 10^{-3}} \right)^{-1} t_K. \quad (36)$$

The ratio of the two timescales is

$$\left(\frac{t_{\text{grow}}}{t_{\text{drift}}} \right)_{\Omega t_s=1} = \frac{4}{3} \sqrt{\frac{4\pi}{3}} \eta \frac{(\rho_{\text{int}} a)_{\Omega t_s=1}}{\Sigma_d} \approx 1 \left(\frac{\eta}{4 \times 10^{-3}} \right) \left(\frac{\Sigma_d / \Sigma_g}{0.01} \right)^{-1} \frac{(\rho_{\text{int}} a)_{\Omega t_s=1}}{\Sigma_g}. \quad (37)$$

The ratio $(t_{\text{grow}}/t_{\text{drift}})_{\Omega t_s=1}$ determines the fate of dust growth at $\Omega t_s = 1$. If $(t_{\text{grow}}/t_{\text{drift}})_{\Omega t_s=1}$ is very small, dust particles

grow beyond $\Omega t_s = 1$ without experiencing significant radial drift; otherwise, dust particles drift inward before they grow. We expect growth without significant drift to occur if

$$\left(\frac{t_{\text{grow}}}{t_{\text{drift}}} \right)_{\Omega t_s=1} \lesssim \frac{1}{30}, \quad (38)$$

where the threshold value $1/30$ takes into account the fact that t_{grow} is the timescale for mass doubling while the particles experience the fastest radial drift over decades in mass. Below, we examine in what condition this requirement is satisfied.

The ratio $(\rho_{\text{int}} a)_{\Omega t_s=1} / \Sigma_g$ depends on the drag regime at $\Omega t_s = 1$. We consider the Epstein regime first. Using $\rho_g = \Sigma_g / (\sqrt{2\pi} h_g)$ and $h_g = c_s/\Omega$, one can rewrite Epstein's law as $\Omega t_s = (\pi/2) \rho_{\text{int}} a / \Sigma_g$. Thus, for $\Omega t_s = 1$, we have a surprisingly simple relation

$$\frac{(\rho_{\text{int}} a)_{\Omega t_s=1}}{\Sigma_g} = \frac{2}{\pi}. \quad (39)$$

Inserting this relation into Equation (35), we obtain

$$t_{\text{grow}}|_{\Omega t_s=1} \approx 30 \left(\frac{\Sigma_d / \Sigma_g}{0.01} \right)^{-1} t_K. \quad (40)$$

Hence, the growth condition (Equation (38)) is not satisfied for the standard disk parameters $\eta \approx 10^{-3}$ and $\Sigma_d / \Sigma_g = 0.01$, in agreement with the results of our and previous (Brauer et al. 2008a) simulations. Note that the right-hand side of Equation (40) is independent of ρ_{int} . Thus, the porosity of aggregates has no effect on the radial drift barrier within the Epstein regime.

The situation differs in the Stokes drag regime. A similar calculation as above leads to

$$\frac{(\rho_{\text{int}} a)_{\Omega t_s=1}}{\Sigma_g} = \frac{9}{2\pi} \frac{\lambda_{\text{mfp}}}{a|_{\Omega t_s=1}} \quad (41)$$

and

$$t_{\text{grow}}|_{\Omega t_s=1} \approx 60 \left(\frac{\Sigma_d / \Sigma_g}{0.01} \right)^{-1} \frac{\lambda_{\text{mfp}}}{a|_{\Omega t_s=1}}. \quad (42)$$

Note that the growth timescale is inversely proportional to the aggregate radius, in contrast to that in the Epstein regime (Equation (40)) being independent of aggregate properties. Substituting Equations (36) and (42) into the growth condition (Equation (38)), we find that aggregates break through the radial drift barrier in the “deep” Stokes regime, $a|_{\Omega t_s=1} / \lambda_{\text{mfp}} \gtrsim 45$. Unlike Equation (40), Equation (42) implicitly depends on ρ_{int} through $a|_{\Omega t_s=1} / \lambda_{\text{mfp}}$ (see below), so the porosity of aggregates does affect the growth timescale in this case. It is interesting to note that the speedup of dust growth occurs even though the maximum collision velocity is the same. Indeed, the collision velocity depends only on Ωt_s and is thus independent of the drag regime. We remark that Stokes' law breaks down when a becomes so large that the particle Reynolds number becomes much larger than unity, as already mentioned in Section 2.2. We will show in Section 5.1 that this fact sets the minimum value of $t_{\text{grow}}|_{\Omega t_s=1}$ to $\approx 0.3 t_K$; see Equation (47).

The internal density of aggregates controls the growth timescale through the aggregate size a at $\Omega t_s = 1$. For given ρ_{int} , one can analytically calculate $a|_{\Omega t_s=1}$ from Equations (39) and (41). Explicitly,

$$a|_{\Omega t_s=1} = \frac{2\Sigma_g}{\pi\rho_{\text{int}}} \quad (43)$$

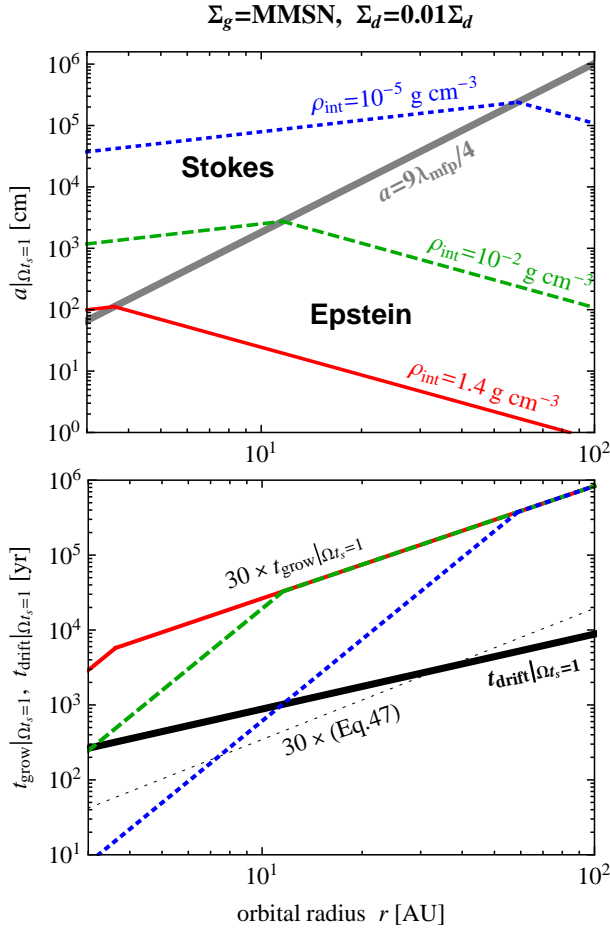


Figure 11. Size a (upper panel) and growth timescale t_{grow} (lower panel) of dust aggregates at $\Omega_{\text{ts}} = 1$ as a function of orbital radius r for internal densities $\rho_{\text{int}} = 1.4 \text{ g cm}^{-3}$ (solid line), $10^{-2} \text{ g cm}^{-3}$ (dashed line), and $10^{-5} \text{ g cm}^{-3}$ (dotted line). The MMSN with the dimensionless diffusion coefficient $\alpha_D = 10^{-3}$ is assumed for the disk model. The thick line in the upper panel indicates $a = 9\lambda_{\text{mfp}}/4$, at which the drag law changes from the Epstein regime to the Stokes regime. The thick line in the lower panel shows the drift timescale $t_{\text{drift}}|_{\Omega_{\text{ts}}=1}$ (independent of ρ_{int}). For $\rho_{\text{int}} = 10^{-5} \text{ g cm}^{-3}$, $t_{\text{grow}}|_{\Omega_{\text{ts}}=1}$ satisfies the growth criterion (Equation (38)) at $r \lesssim 10 \text{ AU}$. In reality, $t_{\text{grow}}|_{\Omega_{\text{ts}}=1}$ does not fall below the value given by Equation (47) (thin dotted line) because of the effect of the gas drag at high particle Reynolds numbers (see Section 5.1). However, this does not change the location where the growth condition is satisfied.

for the Epstein regime, and

$$a|_{\Omega_{\text{ts}}=1} = \frac{3}{(2\pi)^{1/4}} \sqrt{\frac{m_g h_g}{\rho_{\text{int}} \sigma_{\text{mol}}}} \quad (44)$$

for the Stokes regime, where we have used $\lambda_{\text{mfp}} = m_g/(\rho_g \sigma_{\text{mol}})$ and $\rho_g = \Sigma_g/(\sqrt{2\pi} h_g)$. For fixed ρ_{int} , $a|_{\Omega_{\text{ts}}=1}$ decreases with increasing r in the Epstein regime, but increases in the Stokes regime. The upper panel of Figure 11 plots $a|_{\Omega_{\text{ts}}=1}$ for three different values of the aggregate internal density ρ_{int} . If dust particles grew into compact spheres ($\rho_{\text{int}} \sim 1 \text{ g cm}^{-3}$), Epstein's law governs the motion of $\Omega_{\text{ts}} = 1$ particles in almost entire parts of the snow region ($r > 3 \text{ AU}$). However, if dust particles grow into highly porous aggregates with $\rho_{\text{int}} \sim 10^{-5} \text{ g cm}^{-3}$, the particles growing at $r \lesssim 60 \text{ AU}$ enter the Stokes regime before Ω_{ts} reaches unity. The lower panel of Figure 11 shows the two timescales $t_{\text{grow}}|_{\Omega_{\text{ts}}=1}$ and $t_{\text{drift}}|_{\Omega_{\text{ts}}=1}$ as calculated from Equations (35) and (36), respec-

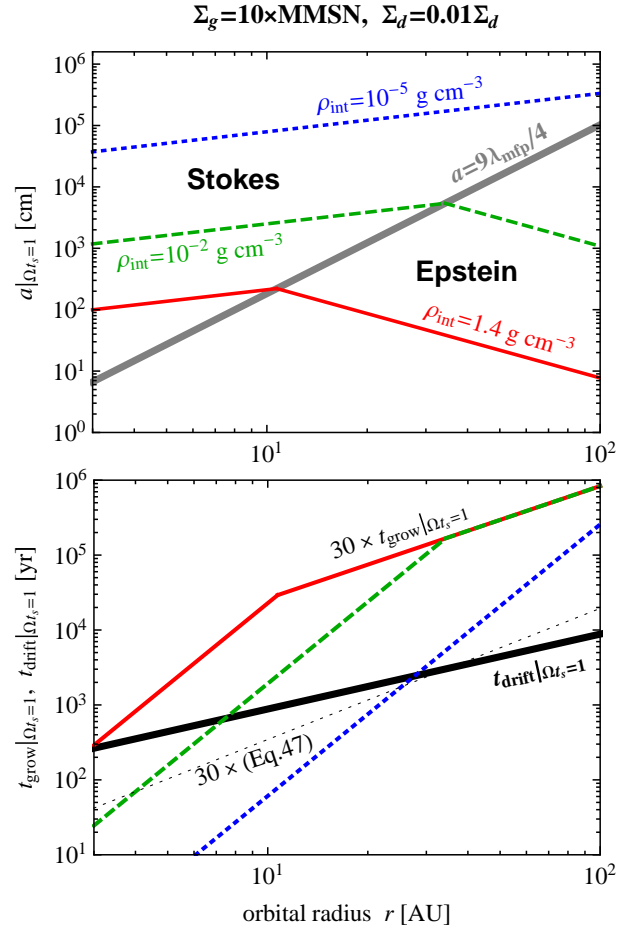


Figure 12. Same as Figure 11, but for a disk 10 times heavier than the MMSN. The growth criterion (Equation (38)) is satisfied at $r \lesssim 25 \text{ AU}$ for $\rho_{\text{int}} = 10^{-5} \text{ g cm}^{-3}$ and at $r \lesssim 7 \text{ AU}$ for $\rho_{\text{int}} = 10^{-2} \text{ g cm}^{-3}$.

tively. We see that compact particles with $\rho_{\text{int}} \sim 1 \text{ g cm}^{-3}$ do not satisfy the growth condition (Equation (38)) outside the snow line, while porous aggregates with $\rho_{\text{int}} \sim 10^{-5} \text{ g cm}^{-3}$ do in the region $r \lesssim 10 \text{ AU}$. These explain our simulation results presented in Section 3.

Finally, we remark that a high disk mass (i.e., a high Σ_g with fixed Σ_d/Σ_g) favors the breakthrough of the radial drift barrier. Figure 12 shows the size a and the timescales t_{grow} and t_{drift} at $\Omega_{\text{ts}} = 1$ for a disk 10 times heavier than the MMSN. We see that the growth condition (Equation (38)) is now satisfied at $r \lesssim 25 \text{ AU}$ for $\rho_{\text{int}} = 10^{-5} \text{ g cm}^{-3}$ and at $r \lesssim 7 \text{ AU}$ even for $\rho_{\text{int}} = 10^{-2} \text{ g cm}^{-3}$. This is because a higher Σ_g leads to a shorter λ_{mfp} and hence allows aggregates to reach the Stokes regime $a/\lambda_{\text{mfp}} \gg 1$ at larger r or with higher ρ_{int} (note that enhancement of Σ_g by a constant remains η and hence $t_{\text{drift}}|_{\Omega_{\text{ts}}=1}$ unchanged). Interestingly, our porosity model predicts that $\rho_{\text{int}}|_{\Omega_{\text{ts}}=1}$ is independent of Σ_g . In fact, substituting Equation (44) with $(\Delta v)_{\Omega_{\text{ts}}=1} \approx \sqrt{\alpha_D} c_s$ and $N_{1+2} \propto \rho_{\text{int}} a^3$ into Equation (28), we obtain the equation for $\rho_{\text{int}}|_{\Omega_{\text{ts}}=1}$ that does not involve Σ_g .

5. DISCUSSION

So far we have shown that the evolution of dust into highly porous aggregates is a key to overcome the radial drift barrier. On the other hand, in order to clarify the role of porosity evolution, we have ignored many other effects relevant to dust growth in protoplanetary disks. In this section, we discuss

how the ignored effects would affect dust evolution.

5.1. Effect of the Friction Law at High Particle Reynolds Numbers

In this study, we have assumed that the stopping time t_s obeys Stokes' law whenever $a \gtrsim \lambda_{\text{mfp}}$. In reality, Stokes' law applies only when the particle Reynolds number (the Reynolds number of the gas flow around the particle) $\text{Re}_p \equiv 2a|v_d - v_g|/\nu_{\text{mol}}$ is less than unity, where $|v_d - v_g|$ is the gas–dust relative velocity. When $\text{Re}_p \gtrsim 1$, i.e., the particle becomes so large and/or the gas–dust relative velocity becomes so high, the stopping time becomes dependent on the particle velocity (see, e.g., Weidenschilling 1977). In this subsection, we discuss how this effect affects our conclusion.

In general, the stopping time at $a \gg \lambda_{\text{mfp}}$ can be written as

$$t_s = \frac{2m}{C_D \rho_g |v_d - v_g| A}, \quad (45)$$

where C_D is a dimensionless coefficient that depends on Re_p . Stokes' law, which applies when $\text{Re}_p \ll 1$, is given by $C_D = 24/\text{Re}_p$. In the opposite limit, $\text{Re}_p \gg 1$, the drag coefficient C_D approaches a constant value (typically of order unity; e.g., $C_D \approx 0.5$ for a sphere with $10^3 \lesssim \text{Re}_p \lesssim 10^5$), which is known as Newton's friction law. Thus, in the Newton regime, the stopping time depends on the particle velocity unlike in the Stokes regime. In this case, one has to calculate the stopping time and particle velocity simultaneously since the particle velocity in turn depends on the stopping time.

In the previous sections, we have ignored the Newton regime to avoid the above-mentioned complexity. However, it is easy to calculate the growth timescale in the Newton regime for given Ωt_s , for which the gas–dust relative velocity can be known in advance. Below, we show that the Newton drag sets the *minimum* value of $t_{\text{grow}}|_{\Omega t_s=1}$ (Equation (35)) for given orbital radius and internal density, which was not taken into account in Section 4. At the midplane, Equation (45) can be rewritten as $\Omega t_s = (2\sqrt{2\pi}/C_D)(c_s/|v_d - v_g|)m/(\Sigma_g A)$, where we have used that $\rho_g = \Sigma_g \Omega / (\sqrt{2\pi} c_s)$. When $\Omega t_s = 1$, the gas–dust relative velocity is dominated by the dust radial velocity $v_r = -\eta v_K$, so we can set $|v_d - v_g| \approx \eta v_K$. Thus, at the midplane, we obtain a relation

$$\frac{(\rho_{\text{int}} a)_{\Omega t_s=1}}{\Sigma_g} \approx \frac{3C_D}{8\sqrt{2\pi}} \frac{\eta v_K}{c_s} \approx 0.07 \left(\frac{C_D}{0.5} \right) \frac{\eta v_K}{c_s}, \quad (46)$$

where we have used that $m/A = 4\rho_{\text{int}} a/3$. If C_D reaches a constant, $(\rho_{\text{int}} a)_{\Omega t_s=1}/\Sigma_g$ no longer depends on aggregate properties. Putting this equation into Equation (35), we have

$$t_{\text{grow}}|_{\Omega t_s=1} \approx 0.3 \left(\frac{\Sigma_d/\Sigma_g}{0.01} \right)^{-1} \left(\frac{C_D}{0.5} \right) \left(\frac{\eta v_K/c_s}{0.08} \right) t_K. \quad (47)$$

When $C_D = 24/\text{Re}_p$, Equation (47) reduces to the equation for the Stokes drag (Equation (42)), where $t_{\text{grow}}|_{\Omega t_s=1}$ decreases with increasing aggregate size a . However, when Re_p becomes so large that C_D reaches a constant value, $t_{\text{grow}}|_{\Omega t_s=1}$ no longer decreases with increasing a . Thus, we find that the Newton drag sets the minimum value of $t_{\text{grow}}|_{\Omega t_s=1}$. For our disk model, in which $\Sigma_d/\Sigma_g = 0.01$ and $\eta v_K/c_s = 0.08(r/5 \text{ AU})^{1/4}$, the minimum growth timescale is $\approx 0.2 - 0.3(C_D/0.5)t_K$ at $r \approx 3 - 10 \text{ AU}$.

Since the Newton drag regime was ignored in our model, the growth rate of aggregates was overestimated there at high

Re_p . As seen in the lower panel of Figure 11, the growth timescale $t_{\text{grow}}|_{\Omega t_s=1}$ for the $\rho_{\text{int}} = 10^{-5} \text{ g cm}^{-3}$ aggregates falls below the minimum possible value given by Equation (47) at $r \lesssim 7 \text{ AU}$. This implies that dust growth is somewhat artificially accelerated in our simulation presented in Section 3.2. However, this artifact is *not* the reason why porous aggregates grow across the radial drift barrier in the simulation. Indeed, the drift timescale $t_{\text{grow}}|_{\Omega t_s=1}$ is $\approx 40t_K$ at these orbital radii, and hence the minimum growth timescale still satisfies the condition for breaking through the drift barrier, Equation (38) (see Section 4). Thus, highly porous aggregates are still able to break through the radial drift barrier even if Newton's law at high particle Reynolds numbers is taken into account.

In summary, we have shown that Newton's friction law ($C_D \approx \text{constant}$) at high particle Reynolds numbers sets a floor value for the grow timescale at $\Omega t_s = 1$. In the numerical simulation presented in Section 3.2, the neglect of the Newton drag regime causes artificial acceleration of the growth of $\Omega t_s \gtrsim 1$ aggregates. However, comparison with the drift timescale shows that the floor value of $t_{\text{grow}}|_{\Omega t_s=1}$ is sufficiently small for dust to grow across $\Omega t_s = 1$. Therefore, the deviation from Stokes' law at high particle Reynolds numbers has little effect on the successful breakthrough of the radial drift barrier observed in our simulation.

5.2. Effects of Frictional Backreaction

So far we have neglected the frictional backreaction from dust to gas when determining the velocities of dust aggregates (Equations (6) and (18)). Here, we discuss the validity of this assumption.

5.2.1. Effect on the Equilibrium Drift Velocity

Frictional backreaction generally modifies the equilibrium velocities of both gas and dust. The equilibrium velocities in the presence of the backreaction are derived by Tanaka et al. (2005) for arbitrary dust size distribution. The result shows that the radial and azimuthal velocities v_r and $v_\phi = v'_\phi + v_K$ of dust particles with stopping time t_s are given by

$$v_r = \frac{1}{1 + (\Omega t_s)^2} v_{g,r} + \frac{2\Omega t_s}{1 + (\Omega t_s)^2} v'_{g,\phi}, \quad (48)$$

$$v'_\phi = -\frac{\Omega t_s}{2[1 + (\Omega t_s)^2]} v_{g,r} + \frac{1}{1 + (\Omega t_s)^2} v'_{g,\phi}, \quad (49)$$

where

$$v_{g,r} = \frac{2Y}{(1+X)^2 + Y^2} \eta v_K, \quad (50)$$

$$v'_{g,\phi} = -\frac{1+X}{(1+X)^2 + Y^2} \eta v_K, \quad (51)$$

are the radial and azimuthal components of the gas velocity relative to the local circular Keplerian motion, respectively, and

$$X = \int \frac{\rho_d(m)}{\rho_g} \frac{1}{1 + (\Omega t_s(m))^2} dm, \quad (52)$$

$$Y = \int \frac{\rho_d(m)}{\rho_g} \frac{\Omega t_s(m)}{1 + (\Omega t_s(m))^2} dm, \quad (53)$$

with $\rho_d(m)$ being the spatial mass density of dust particles per unit aggregate mass.⁵ In the limit of $X, Y \rightarrow 0$, the gas ve-

⁵ Equations (48)–(53) are equivalent to the “multi-species NSH solution” of Bai & Stone (2010a, their Equations (A4) and (A5)).

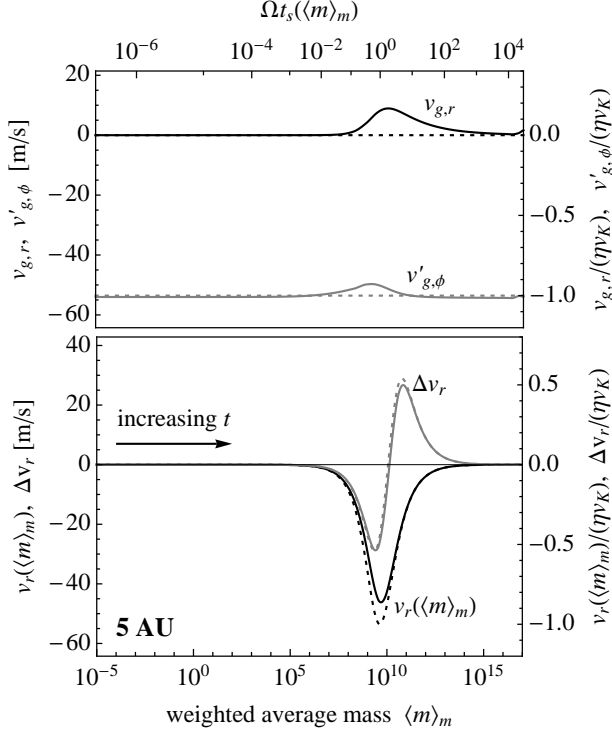


Figure 13. Radial and azimuthal velocities of gas (upper panel) and radial velocity of dust (lower panel) at $r = 5$ AU as a function of the weighted averaged mass $\langle m \rangle_m$. The solid black and gray curves in the upper panel show $v_{g,r}$ and $v'_{g,\phi} = v_{g,\phi} - v_K$, respectively, obtained from the simulation including porosity evolution of aggregates and fractional backreaction from dust to gas. The dotted curves are the velocities when the fractional backreaction is neglected.

locities approach $v_{g,r} \rightarrow 0$ and $v'_{g,\phi} \rightarrow -\eta v_K$, and hence Equations (48) and (49) reduce to Equations (6) and (18), respectively. Thus, the dimensionless quantities X and Y measure the significance of the frictional backreaction. As found from the integrands in Equations (6) and (18), the backreaction is nonnegligible when the local dust-to-gas mass ratio exceeds unity and the aggregates dominating the dust mass tightly couple to the gas.

To test the effect of fractional backreaction, we have also simulated porous aggregation using Equations (48) and (49) instead of Equations (6) and (18) for the aggregate velocities. However, it is found that the effect of backreaction is so small that the resulting dust evolution is hardly distinguishable from that presented in Section 3. The upper panel of Figure 13 shows the temporal evolution of the gas velocities $v_{g,r}$ and $v'_{g,\phi}$ observed in this simulation as a function of the weighted average mass $\langle m \rangle_m$. We see that the observed gas velocities deviate at most only by $9 \text{ m s}^{-1} \approx 0.17 \eta v_K$ from the velocities when the backreaction is absent (dotted lines). As a result of this, the inward velocity $-v_r$ of aggregates with $m = \langle m \rangle_m$ is decreased only by 15 % even when $\Omega t_s(\langle m \rangle_m) \approx 1$ (see the black solid curve in the lower panel of Figure 13). The above result can be understood in the following way. As found from the definitions of X and Y (Equations (52) and (53)), the effect of the backreaction is significant only when the density of dust coupled to the gas ($\Omega t_s \lesssim 1$) is comparable to or higher than the gas density. When $\Omega t_s(\langle m \rangle_m) \lesssim 1$, the density of the coupled dust at the midplane is $\lesssim \Sigma_d/h_d \Omega_{t_s=1} \sim \Sigma_d/(h_g \sqrt{\alpha_D}) \sim (0.01/\sqrt{\alpha_D}) \rho_{g,\text{mid}} \sim 0.3 \rho_{g,\text{mid}} \lesssim \rho_{g,\text{mid}}$, where $\rho_{g,\text{mid}}$ is the midplane gas density and

we have used that $h_d|_{\Omega_{t_s=1}} \sim \sqrt{\alpha_D} h_g \sim 0.03 h_g$ (Equation (3)) and $\Sigma_d/\Sigma_g \approx 0.01$ (the latter is true as long as $\Omega t_s(\langle m \rangle_m) \lesssim 1$). When $\Omega t_s(\langle m \rangle_m) \gtrsim 1$, the dust density does exceed the gas density at the midplane, but the most part of the dust mass is now carried by *decoupled* ($\Omega t_s > 1$) aggregates, which do not affect the gas motion.⁶ Thus, the density of coupled dust is always lower than the gas density, and hence the backreaction effect is insignificant at all times.

Furthermore, the effect on the *differential* drift velocity is even less significant, because the decreases in the inward velocities nearly cancel out. As an example, the gray solid and dotted curves in the lower panel of Figure 13 show the differential radial velocity Δv_r between aggregates of stopping times $t_s = t_s(\langle m \rangle_m)$ and $0.3 t_s(\langle m \rangle_m)$ obtained from the simulations with and without the backreaction, respectively. We see that the maximum values of $|\Delta v_r|$, which are reached when $\Omega t_s(\langle m \rangle_m) \approx 0.7$, differ only by 5%. Therefore, the frictional backreaction from dust to gas hardly affects the drift-induced collision velocity between dust aggregates.

5.2.2. Streaming Instability

The backreaction of dust on gas causes another phenomenon, the so-called streaming instability (Youdin & Goodman 2005). This means that the equilibrium gas–dust motion as described by Equations (6)–(18) is unstable against perturbation. One important consequence of this instability is rapid clumping of marginally decoupled ($\Omega t_s \sim 1$) dust particles (e.g., Johansen & Youdin 2007; Johansen et al. 2007; Bai & Stone 2010a). The clumping proceeds in a runaway manner (i.e., turbulent diffusion no longer limits the clumping) once the dust density exceeds the gas density at the midplane (e.g., Johansen & Youdin 2007; see also the analytic explanation of this by Johansen et al. 2009). The runaway clumps could be eventually gravitationally bound and form 100 km sized planetesimals (Johansen et al. 2007). For more tightly coupled ($\Omega t_s \ll 1$) particles, however, the clumping occurs only moderately unless the dust-to-gas surface density ratio is high and/or the radial drift speed is low (Johansen et al. 2009; Bai & Stone 2010b). This is also true for loosely coupled particles ($\Omega t_s \gg 1$) for which the interaction with the gas is weak.

As seen in Section 3.2, porous aggregates are able to reach $\Omega t_s \sim 1$ in inner regions of disks. These aggregates likely trigger the streaming instability and can even experience runaway collapse. However, it is not obvious whether the clumps really experience the runaway collapse, since the growth timescale of the $\Omega t_s \sim 1$ aggregates can be as short as one orbital period (see Section 5.1), which is comparable to the growth time of the streaming instability at $\Omega t_s = 1$ (Youdin & Goodman 2005). If the aggregates cross $\Omega t_s \sim 1$ faster than the clumps develop, planetesimal formation will occur via direct collisional growth rather than gravitational instability. In order to address this issue, we will need to simulate coagulation and streaming instability simultaneously.

5.3. Fragmentation Barrier

In this study, we have assumed that all aggregate collisions lead to sticking. This assumption breaks down if the collisional velocity is so high that the collision involves fragmentation and erosion. If the mass loss due to fragmentation and

⁶ Indeed, X and Y are insensitive to $\Omega t_s \gg 1$ particles because the factors $1/[1 + (\Omega t_s)^2] \approx t_s^{-2}$ and $\Omega t_s/[1 + (\Omega t_s)^2] \approx t_s^{-1}$ decrease faster than the spatial dust density $\rho_d \propto \Sigma_d/h_d \propto t_s^{1/2}$ increases (see Equation (3)).

erosion is significant, it acts as an obstacle to planetesimal formation (the so-called fragmentation barrier; e.g., Brauer et al. 2008a). Here, we discuss the validity and possible limitations of this assumption.

Recent N -body simulations predict that very fluffy aggregates made of $0.1 \mu\text{m}$ sized icy particles experience catastrophic disruption at collision velocities $\Delta v \gtrsim 35 \text{ m s}^{-1}$ (Wada et al. 2009). If a large aggregate grows mainly through collisions with similar-sized ones (which is true in our simulations; see Figure 9), the collision velocity at $\Omega t_s \approx 1$ is dominated by the turbulence-driven velocity $\Delta v_i \approx \delta v_g \approx \sqrt{\alpha_D} c_s$ (Section 2.3.2). If the disk is optically thin and moderately turbulent ($\alpha_D = 10^{-3}$) as in our model, the collision velocity is $\approx 21 \text{ m s}^{-1}$ at $r = 5 \text{ AU}$, so catastrophic disruption is likely insignificant for such collisions. However, if turbulence is as strong as $\alpha_D = 10^{-2}$, the collision velocity at $r = 5 \text{ AU}$ and $\Omega t_s = 1$ goes up to 67 m s^{-1} . In protoplanetary disks, strong turbulence with $\alpha_D \gtrsim 10^{-2}$ can be driven by magnetorotational instability (MRI; e.g., Balbus & Hawley 1998). If such strong turbulence exists, fragmentation becomes no more negligible even for icy aggregates. Besides, the collision velocity can become higher than the above estimate when a large aggregate collides with much smaller ones, since the collision velocity is then dominated by the radial drift motion. For example, the differential radial drift velocity between an $\Omega t_s = 1$ aggregate and a much smaller one is as high as $\approx \eta v_K \approx 56 \text{ m s}^{-1}$ in optically thin disks. At such a high velocity, erosion by small aggregates can also slow down the growth of $\Omega t_s \approx 1$ aggregates, although net growth might be possible (see, e.g., Teiser & Wurm 2009; Teiser et al. 2011).

On the other hand, resupply of small dust particles by fragmentation/erosion has positive effects on dust growth. First, small dust particles stabilize MRI-driven turbulence because they efficiently capture ionized gas particles and thereby reduce the electric conductivity of the gas (e.g., Sano et al. 2000). This process generally leads to the reduction of the gas random velocity (and hence the reduction of turbulence-induced collision velocity), especially when the magnetic fields threading the disk are weak (Okuzumi & Hirose 2011). In addition, small fragments enhance the optical thickness of the disk, and thus reduce the temperature of the gas in the interior of the disk (given that turbulence is stabilized there). Since the radial drift velocity is proportional to the gas temperature, this leads to the reduction of the drift-induced collision velocity. In the limit of large optical depths, the gas temperature is reduced by a factor $\approx (h/r)^{1/4} \approx 0.5$ near the midplane (Kusaka et al. 1970), resulting in the reduction of the drift-induced collision velocity to 28 m s^{-1} . These effects may help the growth of large aggregates beyond the fragmentation barrier.

The size of monomers is another key factor. Although we have assumed monodisperse monomers of $a_0 = 0.1 \mu\text{m}$, the size of interstellar dust particles ranges from nanometers to microns. It is suggested both theoretically (Chokshi et al. 1993; Dominik & Tielens 1997) and experimentally (Blum & Wurm 2008) that the threshold velocity for sticking is roughly inversely proportional to a_0 . Thus, inclusion of larger monomers generally leads to the decrease in the sticking efficiency. However, it is not obvious whether aggregates composed of multi-sized interstellar particles are mechanically weaker or stronger than aggregates considered in this study. For example, if the monomer size distribution dn_0/da_0 obeys that of interstellar dust particles,

$dn_0/d \log a_0 \propto a_0^{-5/2}$ (Mathis et al. 1977), the total mass of the aggregates is dominated by the largest ones ($m_0 \propto a_0^3$ and hence $m_0 dn_0/d \log a_0 \propto a_0^{1/2}$). Nevertheless, the existence of smaller monomers can still be important, since the binding energy per contact E_{break} is proportional to $a_0^{4/3}$ (Chokshi et al. 1993; Dominik & Tielens 1997) and hence the total binding energy tends to be dominated by the smallest ones ($E_{\text{break}} dn_0/d \log a_0 \propto a_0^{-7/6}$). The net effect of multi-sized monomers needs to be clarified by future numerical as well as laboratory experiments.

Another issue about the growth efficiency of icy aggregates arises from sintering. Sintering is redistribution of ice molecules on solid surfaces due to vapor transport and other effects. In this process, ice molecules tend to fill dipped surfaces (i.e., surfaces with negative surface curvature) since the equilibrium vapor pressure decreases with decreasing the surface curvature. In an aggregate composed of equal-sized icy monomers, this process leads to growth of the monomer contact areas (Sirono 2011b) and consequently to enhancement of the aggregate's mechanical strength such as F_{roll} . Significant growth of the contact areas could cause the reduction of the aggregate's sticking efficiency since the dissipation of the collision energy through internal rolling/sliding motion could then be suppressed (Sirono 1999). Furthermore, if the monomers have different sizes, sintering leads to evaporation of smaller monomers (having higher positive curvature), which may result in the breakup of the aggregate (Sirono 2011a). Therefore, sintering can prevent the growth of icy aggregates near the snow line where sintering proceeds rapidly. Sirono (2011b) shows that the timescale of H_2O sintering falls below 10^3 yr in the region between the snow line (3 AU) and 7 AU for the radial temperature adopted in our study. This is comparable to the timescale on which submicron-sized icy particles grow into macroscopic objects in this region (see Figure 7). However, if the disk is passive and optically thick (Kusaka et al. 1970), no icy materials (including H_2O and CO_2) undergo rapid sintering at $r \gtrsim 4 \text{ AU}$ (Sirono 2011b). Moreover, the required high optical depth can be provided by tiny fragments that would result from the sintering-induced fragmentation itself. Consistent treatment of the two competing effects is necessary to precisely know the location where sintering is really problematic.

To summarize, whether icy aggregates survive catastrophic fragmentation and erosion crucially depends on the environment of protoplanetary disks as well as on the size distribution of the aggregates and constituent monomers. However, we emphasize that icy aggregates can survive within a realistic range of disk conditions as explained above. Indeed, the range is much wider than that for rocky aggregates, for which catastrophic disruption occurs at collision velocities as low as a few m s^{-1} (Blum & Wurm 2008; Wada et al. 2009; Güttler et al. 2010). In order to precisely predict in what conditions icy aggregates overcome the fragmentation barrier, we need to take into account the mass loss due to fragmentation/erosion and the reduction of collision velocities due to the resupply of small particles in a self-consistent way. This will be done in our future work.

5.4. Validity and Limitations of the Porosity Model

Aggregates observed in our simulation have very low internal densities. This is a direct consequence of the porosity model we adopted (Equation (15)). Here, we discuss the validity and limitations of our porosity model.

As mentioned in Section 2.3.1, our porosity change recipe at $E_{\text{imp}} \geq E_{\text{roll}}$ is based on head-on collision experiments of similar-sized aggregates. In our simulation, dust growth is indeed dominated by collision with similar-sized aggregates (see Section 3.2.1), so our result is unlikely affected by the limitation of the porosity model regarding the size ratio. By contrast, the neglect of offset collision may cause underestimation of the porosity increase, since the impact energy is spent for stretching rather than compaction at offset collision (Wada et al. 2007; Paszun & Dominik 2009). If this is the case, then the breakthrough of the radial drift barrier can occur even outside 10 AU.

On the other hand, the formation of low-density dust aggregates is apparently inconsistent with the existence of massive and much less porous aggregates in our solar system. For example, comets, presumably the most primitive dust “aggregates” in the solar system, are expected to have mean internal densities of $\rho_{\text{int}} \sim 0.1 \text{ g cm}^{-3}$ (e.g., Greenberg & Hage 1990). Since our porosity model does not explain the formation of such large and less porous “aggregates,” there should exist any missing compaction mechanisms.

One possibility is *static* compression due to gas drag and self-gravity. Although static compression is ignored in our porosity model, it can contribute to compaction of aggregates that are massive or decoupled from the gas motion. For relatively compact ($\rho_{\text{int}} \sim 0.1 \text{ g cm}^{-3}$) dust cakes made of micron-sized SiO_2 particles, static compaction is observed to occur at static pressure $> 100 \text{ Pa}$ (Blum & Schräpler 2004; Güttler et al. 2009). By contrast, the static compression strength has not yet been measured so far for icy aggregates with very low internal densities ($\rho_{\text{int}} \ll 0.1 \text{ g cm}^{-3}$). However, for future reference, it will be useful to estimate here the static pressures due to gas drag and self-gravity.

The ram pressure, the gas drag force per unit area, is given by $P_{\text{ram}} = C_D \rho_g |v_d - v_g|^2 / 2$, where C_D is the drag coefficient and $|v_d - v_g|$ is the gas–dust relative speed (see Section 5.1). At $\Omega t_s \gtrsim 1$, the gas–dust relative speed is approximately equal to ηv_K . Thus, assuming Newton’s drag law $C_D \sim 1$ for $\Omega t_s \gtrsim 1$ aggregates (Section 5.1), the ram pressure at $\Omega t_s \gtrsim 1$ is estimated as

$$P_{\text{ram}} \sim \rho_g (\eta v_K)^2 \sim 10^{-5} \left(\frac{\rho_g}{10^{-11} \text{ g cm}^{-3}} \right) \left(\frac{\eta v_K}{50 \text{ m s}^{-1}} \right)^2 \text{ Pa} \quad (54)$$

independently of aggregate properties. Thus, if the static compression strength of our high porous aggregates is lower than 10^{-5} Pa , compression of the aggregates will occur at $\Omega t_s \gtrsim 1$ due to ram pressure.

The static pressure due to self-gravity is estimated from dimensional analysis as

$$P_{\text{grav}} \sim \frac{Gm^2}{a^4} \sim 10^{-7} \left(\frac{m}{10^{10} \text{ g}} \right)^{2/3} \left(\frac{\rho_{\text{int}}}{10^{-5} \text{ g cm}^{-3}} \right)^{4/3} \text{ Pa}. \quad (55)$$

For $m \sim 10^{10} \text{ g}$ and $\rho_{\text{int}} \sim 10^{-5} \text{ g cm}^{-3}$, which correspond to the $\Omega t_s = 1$ aggregates observed in our simulation (Figure 5), the gravitational pressure is much weaker than the ram pressure. However, since $P_{\text{grav}} \propto m^{2/3}$, compression due to self-gravity becomes important for much heavier aggregates. For example, if $\rho_{\text{int}} \sim 10^{-5} (m/10^{10} \text{ g})^{-1/5} \text{ g cm}^{-3}$ as is for the $\Omega t_s \gtrsim 1$ aggregates observed in our simulation, P_{grav} exceeds P_{ram} at $m \sim 10^{17} \text{ g}$, which is comparable to the mass of comet Halley. Moreover, since $P_{\text{grav}} \propto \rho_{\text{int}}^{4/3}$, gravitational compaction will proceed in a runaway manner unless

the static compression strength increases more rapidly than P_{grav} . Thus, static compression due to self-gravity may be a key to fill the gap between our high porous aggregates and more compact planetesimal-mass bodies in the solar system.

6. SUMMARY AND OUTLOOK

We have investigated how the porosity evolution of dust aggregates affects their collisional growth and radial inward drift. We have applied a porosity model based on N -body simulations of aggregate collisions (Suyama et al. 2008, 2012). This porosity model allows us to study the porosity change upon collision for a wide range of impact energies. As a first step, we have neglected the mass loss due to collisional fragmentation and instead focused on dust evolution outside the snow line, where aggregates are mainly composed of ice and hence catastrophic fragmentation may be insignificant (Wada et al. 2009). Our findings are summarized as follows.

1. Icy aggregates can become highly porous even if collisional compression is taken into account (Section 3.2). Our model calculation suggests that the internal density of icy aggregates at 5 AU falls off to $10^{-5} \text{ g cm}^{-3}$ by the end of the initial fractal growth stage and then is kept to this level until the aggregates decouple from the gas motion (Figure 10). Stretching of merged aggregates at offset collisions, which is not taken into account in our porosity model, could further decrease the internal density (Wada et al. 2007; Paszun & Dominik 2009).
2. A high porosity triggers significant acceleration in collisional growth. This acceleration is a natural consequence of particles’ aerodynamical property in the Stokes regime, i.e., at particle radii larger than the mean free path of the gas molecules (Section 4). The porosity (or internal density) of an aggregate determines whether the aggregate reaches the Stokes regime before the radial drift stalls its growth. Compact aggregates tend to drift inward before experiencing the rapid growth, while highly porous aggregates are able to experience it over a wide range of the orbital radius (Figure 11).
3. The growth acceleration enables the aggregates to overcome the radial drift barrier in inner regions of the disks. Our model calculation shows that the breakthrough of the radial drift barrier can occur at orbital radii less than 10 AU in the MMSN (Figure 5). A higher disk mass allows this to occur at larger orbital radii or higher internal densities (Figure 12). The radial drift barrier has been commonly thought to be one of the most serious obstacles against planetesimal formation. Our result suggests that, if the fragmentation of icy aggregates is truly insignificant (see Section 5.3), formation of icy planetesimals is possible via direct collisional growth of submicron-sized icy particles even without an enhancement of the initial dust-to-gas mass ratio.
4. Further out in the disk, the growth of porous icy aggregates is still limited by the radial drift barrier, but their inward drift results in enhancement of the dust surface density in the inner region (Figure 6). This enhancement may help the core of giant planets to form within a disk lifetime (Kobayashi et al. 2010, 2011).

We remark that the quick growth in the Stokes regime was also observed in recent coagulation simulations by Birnstiel et al. (2010, see their Figure 11) and Zsom et al. (2011, see their Figure 3). Birnstiel et al. (2010) observed the breakthrough of the radial drift barrier only at small orbital radii ($r \lesssim 0.5$ AU) since they assumed compact aggregation. Zsom et al. (2011) found rapid growth of porous aggregates in the Stokes regime, but did not consider the loss of the dust surface density through radial drift. What we have clarified in this study is that porosity evolution indeed enables the breakthrough of the radial drift barrier at much larger orbital radii.

The porosity evolution can even influence the evolution of solid bodies after planetesimal formation. It is commonly believed that the formation of protoplanets begins with the runaway growth of a small number of planetesimals due to gravitational focusing (e.g., Wetherill & Stewart 1989). The runaway growth requires a sufficiently high gravitational escape velocity $v_{\text{esc}} = \sqrt{2Gm/a}$ relative to the collision velocity. Since the escape velocity decreases with decreasing internal density ($v_{\text{esc}} \propto m^{1/3} \rho_{\text{int}}^{1/6}$), it is possible that a high porosity delays the onset of the runaway and thereby affects its outcome. For example, a recent protoplanet growth model including collisional fragmentation/erosion (Kobayashi et al. 2010, 2011) suggests that planetesimals need to have grown to $> 10^{21}$ g before the runaway growth begins in order to enable the formation of gas giant planets within the framework of the core accretion scenario (Mizuno 1980; Pollack et al. 1996). The size of the “initial” planetesimals can even determine the mass distribution of asteroids in the main belt (Morbidelli et al. 2009; Weidenschilling 2011). As we pointed out in Section 5.4, compaction of large and massive aggregates may occur through static compression due to gas drag or self gravity. To precisely determine when it occurs is beyond the scope of this work, but it will be thus important to understand later stages of planetary system formation. We will address this in future work.

The authors thank the anonymous referee for useful comments. We also thank Tilman Birnstiel, Frithjof Brauer, Cornelis Dullemond, Shu-ichiro Inutsuka, Chris Ormel, Taku Takeuchi, Takayuki Tanigawa, Fredrik Windmark, and Andras Zsom for fruitful discussions. S.O. acknowledges support by Grants-in-Aid for JSPS Fellows (22 · 7006) from MEXT of Japan.

REFERENCES

- Adachi, I., Hayashi, C., & Nakazawa, K. 1976, *Prog. Theor. Phys.*, 56, 1756
- Bai, X.-N., & Stone, J. 2010a, *ApJ*, 722, 1437
- Bai, X.-N., & Stone, J. 2010b, *ApJ*, 722, L220
- Balbus, S. A., & Hawley, J. F. 1998, *Rev. Mod. Phys.*, 70, 1
- Barge, P., & Sommeria, J. 1995, *A&A*, 295, L1
- Birnstiel, T., Dullemond, C. P., & Brauer, F. 2009, *A&A*, 503, L5
- Birnstiel, T., Dullemond, C. P., & Brauer, F. 2010, *A&A*, 513, 79
- Birnstiel, T., Klahr, H., & Ercolano, B. 2012, *A&A*, 539, A148
- Blum, J. 2004, in *ASP Conf. Ser. 309, Astrophysics of Dust*, ed. A. N. Witt, G. C. Clayton, & B. T. Draine (San Francisco, CA: ASP), 369
- Blum, J., & Schräpler, R. 2004, *Phys. Rev. Lett.*, 93, 115503
- Blum, J., & Wurm, G. 2000, *Icarus*, 143, 138
- Blum, J., & Wurm, G. 2008, *ARA&A*, 46, 21
- Brauer, F., Dullemond, C. P., & Henning, Th. 2008a, *A&A*, 480, 859
- Brauer, F., Henning, Th., & Dullemond, C. P. 2008b, *A&A*, 487, L1
- Chokshi, A., Tielens, A. G. G. M., & Hollenbach, D. 1993, *ApJ*, 407, 806
- Dominik, C., & Tielens, A. G. G. M. 1995, *Phil. Mag. A*, 72, 783
- Dominik, C., & Tielens, A. G. G. M. 1997, *ApJ*, 480, 647
- Dubrunelle, B., Morfill, G., & Sterzik, M. 1995, *Icarus*, 114, 237
- Dubrunelle, B., & Valdettaro, L. 1992, *A&A*, 263, 387
- Fromang, S., & Papaloizou, J. 2006, *A&A*, 452, 751
- Goldreich, P., & Ward, W. R. 1973, *ApJ*, 183, 1051
- Greenberg, J. M., & Hage, J. I. 1990, *ApJ*, 361, 260
- Gundlach, B., Kiliyas, S., Beitz, E., & Blum, J. 2011, *Icarus*, 214, 717
- Güttler, C., Blum, J., Zsom, A., Ormel, C. W., & Dullemond, C. P. 2010, *A&A*, 513, A56
- Güttler, C., Krause, M., Geretshauser, R. J., Speith, R., & Blum, J. 2009, *ApJ*, 701, 130
- Hayashi, C. 1981, *Prog. Theor. Phys. Suppl.*, 70, 35
- Hayashi, C., Nakazawa, K., & Nakagawa, Y. 1985, in *Protostars and Planets II*, ed. D. C. Black & M. S. Matthews (Tucson, AZ: Univ. Arizona Press), 1100
- Hirose, S., & Turner, N. J. 2011, *ApJ*, 732, L30
- Johansen, A., Klahr, H., & Mee, A. J. 2006, *MNRAS*, 370, L71
- Johansen, A., Oishi, J. S., Mac Low, M.-M., et al. 2007, *Nature*, 448, 1022
- Johansen, A., & Youdin, A. 2007, *ApJ*, 662, 627
- Johansen, A., Youdin, A., & Mac Low, M.-M. 2009, *ApJ*, 704, L75
- Klahr, H. H., & Henning, T. 1997, *Icarus*, 128, 213
- Kobayashi, H., Tanaka, H., & Krivov, A. V. 2011, *ApJ*, 738, 35
- Kobayashi, H., Tanaka, H., Krivov, A. V., & Inaba, S. 2010, *Icarus*, 209, 836
- Kretke, K. A., & Lin, D. N. C. 2007, *ApJ*, 664, L55
- Kusaka, T., Nakano, T., & Hayashi, C. 1970, *Prog. Theor. Phys.*, 44, 1580
- Langkowski, D., Teiser, J., & Blum, J. 2008, *ApJ*, 675, 764
- Mathis, J. S., Rimpl, W., & Nordsieck, K. H. 1977, *ApJ*, 217, 425
- Mathews, L. S., Land, V., & Hyde, T. W. 2012, *ApJ*, 744, 8
- Mizuno, H. 1980, *Prog. Theor. Phys.*, 64, 544
- Morbidelli, A., Bottke, W. F., Nesvorný, D., & Levison, H. F. 2009, *Icarus*, 204, 558
- Mukai, T., Ishimoto, H., Kozasa, T., Blum, J., & Greenberg, J. M. 1992, *A&A*, 262, 315
- Nakagawa, Y., Nakazawa, K., & Hayashi, C. 1981, *Icarus*, 45, 517
- Nakagawa, Y., Sekiya, M., & Hayashi, C., 1986, *Icarus*, 67, 375
- Okuzumi, S. 2009, *ApJ*, 698, 1122
- Okuzumi, S., & Hirose, S. 2011, *ApJ*, 742, 65
- Okuzumi, S., Tanaka, H., & Sakagami, M.-a. 2009, *ApJ*, 707, 1247
- Okuzumi, S., Tanaka, H., Takeuchi, T., & Sakagami, M.-a., 2011a, *ApJ*, 731, 95
- Okuzumi, S., Tanaka, H., Takeuchi, T., & Sakagami, M.-a., 2011b, *ApJ*, 731, 96
- Ormel, C. W., & Cuzzi, J. N. 2007, *A&A*, 466, 413
- Ormel, C. W., Spaans, M., & Tielens, A. G. G. M. 2007, *A&A*, 461, 215
- Paszun, D., & Dominik, C. 2009, *A&A*, 507, 1023
- Pinilla, P., Birnstiel, T., Ricci, L., et al. 2012, *A&A*, 538, A114
- Pollack, J. B., Hubickyj, O., Bodenheimer, P., et al. 1996, *Icarus*, 124, 62
- Safronov, V. S. 1969, *Evolution of the Protoplanetary Cloud and Formation of the Earth and the Planets* (Moscow: Nauka)
- Sano, T., Miyama, S. M., Umebayashi, T., & Nakano, T. 2000, *ApJ*, 543, 486
- Sekiya, M. 1998, *Icarus*, 133, 298
- Shakura, N. I., & Sunyaev, R. A. 1973, *A&A*, 24, 337
- Sirono, S. 1999, *A&A*, 347, 720
- Sirono, S. 2011a, *ApJ*, 733, L41
- Sirono, S. 2011b, *ApJ*, 735, 131
- Suyama, T., Wada, K., & Tanaka, H. 2008, *ApJ*, 684, 1310
- Suyama, T., Wada, K., Tanaka, H., & Okuzumi, S. 2012, *ApJ*, in press (arXiv:1205.1894)
- Suzuki, T. K., Muto, T., & Inutsuka, S. 2010, *ApJ*, 718, 1289
- Tanaka, H., Himeno, Y., & Ida, S. 2005, *ApJ*, 625, 414
- Teiser, J., Küpper, M., & Wurm, G. 2009, *Icarus*, 215, 596
- Teiser, J., & Wurm, G. 2009, *MNRAS*, 393, 1584
- Toomre, A. 1964, *ApJ*, 139, 1217
- Turner, N. J., Carballido, A., & Sano, T. 2010, *ApJ*, 708, 188
- Wada, K., Tanaka, H., Suyama, T., Kimura, H., & Yamamoto, T. 2007, *ApJ*, 661, 320
- Wada, K., Tanaka, H., Suyama, T., Kimura, H., & Yamamoto, T. 2008, *ApJ*, 677, 1296
- Wada, K., Tanaka, H., Suyama, T., Kimura, H., & Yamamoto, T. 2009, *ApJ*, 702, 1490
- Wada, K., Tanaka, H., Suyama, T., Kimura, H., & Yamamoto, T. 2011, *ApJ*, 737, 36
- Weidenschilling, S. J. 1977, *MNRAS*, 180, 57
- Weidenschilling, S. J. 2011, *Icarus*, 214, 671
- Weidenschilling, S. J., & Cuzzi, J. N. 1993, in *Protostars and Planets III*, ed. E. H. Levy & J. I. Lunine (Tucson, AZ: Univ. Arizona Press), 1031
- Weidling, R., Güttler, C., Blum, J., & Brauer, F. 2009, *ApJ*, 696, 2036
- Wetherill, G. W., & Stewart, G. R. 1989, *Icarus*, 77, 330
- Whipple, F. L. 1972, in *From Plasma to Planet*, ed. A. Elvius (New York: Wiley Interscience), 211
- Windmark, F., Birnstiel, T., Güttler, C., et al. 2012, *A&A*, 540, A73
- Youdin, A. N., & Goodman, J. 2005, *ApJ*, 620, 459
- Youdin, A. N., & Lithwick, Y. 2007, *Icarus*, 192, 588
- Zsom, A., Ormel, C. W., Dullemond, C. P., & Henning, T. 2011, *A&A*, 534, A73
- Zsom, A., Ormel, C. W., Güttler, C., Blum, J., & Dullemond, C. P. 2010, *A&A*, 513, A57